Incorporating Planar Qubits and Resonators in circuit Quantum Acoustodynamics

Master Thesis

S. Raamamurthy

20th August 2023

Advisors: Prof. Dr. Yiwen Chu, Dr. Ines C. Rodrigues

Laboratory for Solid State Physics, D-PHYS, ETH Zürich

Abstract

The interplay of mechanical resonators and superconducting circuits is being explored as the basis of a platform for the storage, manipulation and transduction of quantum states, forming the basis of the field of circuit quantum acoustodynamics. The setup used in the Hybrid Quantum Systems group uses a 3D superconducting cavity to fill the role of the electromagnetic resonator for dispersive readout. We demonstrate the implementation of a 2D architecture using coplanar waveguide resonators and planar qubits, and study the design challenges and advantages introduced by this approach. Through this work, we open the door to introducing alternate system control methods, as well as scaling up the architecture to provide a robust hybrid system for quantum computing.

Acknowledgements

As I think about the last few months, and the challenges faced across this project, I am obliged to thank the many people responsible for this project's success. I first would like to thank Professor Yiwen Chu for giving me this unique opportunity, that has entirely changed my perspective and career direction. I am deeply indebted to Dr. Ines C. Rodrigues for all of her patience and tutelage, as well as Yu Yang, for all of his support and training in the cleanroom. I cannot overstate the appreciation I have for the time and energy they invested in this project. Additionally, I extend my sincere thanks to Marius Bild, Andraz Omahen, Dr. Rodrigo Benevides, Stefan Pfleging, and all others involved in the design, fabrication and measurement of our devices, as well as to the rest of the group for their advice and friendship over the course of this project.

Finally, I thank my family for their support and patience during this hectic time. All of this would not be possible without them.

Contents

Chapter 1

Introduction

Mechanical resonators are currently being explored as potential quantum devices in a number of applications, such as sensing [2], logical operations and storage [3]. These systems offer unique advantages, such as their resilience against electromagnetic noise and their ability to couple through gravitational forces; and their operation as macroscopic oscillators in the quantum regime is of great theoretical interest. By coupling them to superconducting circuits,
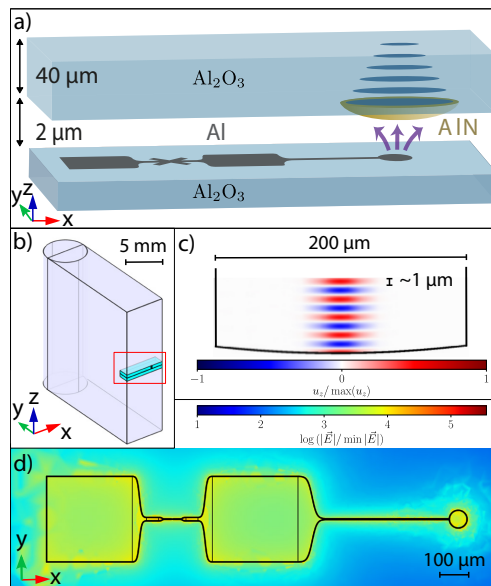
Figure 1.1: Adapted from Banderier, Drimmer, Chu (2023) [1]. a) The setup currently used in the Hybrid Quantum Systems group, featuring the qubit, piezoelectric dome (AlN) and HBAR (upper block). b) The location of the device in the cavity. Only half the cavity is shown for clarity; the cavity is symmetrical, and the device is in the center. c) The fundamental mode in the HBAR, illustrated using the displacement field of the mode. d) The electric field of the qubit mode around the transmon.

often through piezoelectric materials, we can exert control over these systems and simultaneously benefit from the versatility of microelectronic devices.

The research performed at the Hybrid Quantum Systems group explores one such combination of mechanical and electronic devices, illustrated in Figure 1.1 [4, 5]. The role of the mechanical resonator is filled by a high-overtone bulk acoustic resonator (HBAR), and the role of electronic control is filled by a superconducting qubit and cavity. This three-component system is referred to as the $\hbar$BAR, and its behaviour is described by the interaction of quantum acoustics and cavity quantum electrodynamics (QED). The work done with this and other hybrid superconducting/mechanical systems forms the basis of the field of circuit quantum acoustodynamics (cQAD), and such devices lend itself to a number of protocols, such as the creation of cat states [6].

This project was motivated by the limitations of superconducting cavities and their role in this arrangement. 3D cavities are a staple for QED devices and experiments due to their many advantages, including high quality factors and innate modularity [7]. However, their nature also limits the ability to control the different components of this system. We propose to move from 3D to 2D implementations of superconducting cavities for these hybrid systems, replacing them with 2D resonators – a move that will open the door to new tools for qubit and mechanical control (such as flux bias lines and phonon drive lines), new loss mitigation mechanisms, and the scaling up of these hybrid architectures.

Over the course of this thesis, we provide an overview of the theory and techniques used across this project. We begin in Section 2 with a summary of circuit QED and the concepts involved in qubit and resonator design and control. We then dive into the actual task of qubit design in Section 3, demonstrating the qubit designs we work with and how to tune them to achieve our desired properties. Finally, we discuss the process of device fabrication, and the results achieved during this project, in Section 4.

Chapter 2

Superconducting Qubit Theory

In this chapter, we explore the main concepts of superconducting qubits and coplanar waveguides. We then discuss the behaviour of a qubit coupled to a resonator, starting with the Jaynes-Cummings model, and leading up to the uses of a resonator as a control and readout mechanism for superconducting qubits.

2.1 A Review of Superconducting Qubits

We begin this section with a review on superconducting qubits, and the concepts used throughout this project.

2.1.1 The Quantum Harmonic Oscillator

To motivate the development of superconducting qubits, we first consider the properties of the classical LC circuit – that is, a circuit composed of a parallel inductance and capacitance. The Hamiltonian of the LC circuit is given by

$$\mathcal{H} = \frac{Q^2}{2C} + \frac{\Phi^2}{2L} = \frac{Q^2}{2C} + C\left(\frac{1}{\sqrt{LC}}\right)^2 \frac{\Phi^2}{2},$$ (2.1)

where C represents the circuit capacitance, Q the charge on this capacitor and Φ the flux crossing the inductor. We note that Q and Φ function as classical conjugate variables, as evidenced by the Poisson bracket $\{\Phi, Q\} = 1$. As such, we conclude that this Hamiltonian is analogous to that of a mechanical harmonic oscillator, which takes the form $\mathcal{H} = p^2/2m + m\omega^2 x^2/2$, with x and p describing the classical conjugates variables of position and momentum, m the oscillator mass, and ω the resonance frequency. Comparing these two equations and their variables, we can extract the analogous oscillator frequency $\omega = 1/\sqrt{LC}$.

We can convert the classical Hamiltonian into its quantum-mechanical analogue by replacing Q and Φ with their operators (for convenience, we omit the operator hats). We can go further, and replace these operators with more intuitive choices for superconducting circuits, taking the *reduced charge* $n = Q/2e$ and *reduced flux* $\varphi = 2\pi\Phi/\Phi_0$. ($\Phi_0$ here is the magnetic flux quantum $h/2e$.) The formulation of the reduced charge term is chosen to reflect the role of Cooper pairs as the main charge carriers in superconducting circuits.

With these operators, the quantum mechanical Hamiltonian becomes [8]

$$H = \frac{4e^2 n^2}{2C} + \frac{\left(\frac{\Phi_0}{2\pi}\right)^2 \varphi^2}{2L} = 4E_\text{C} n^2 + \frac{1}{2} E_\text{L} \varphi^2, \tag{2.2}$$

where $E_\text{C} = e^2/2C$ is referred to as the *charging energy*, and $E_\text{L} = (\Phi_0/2\pi)^2/L$ the *inductive energy*. We can further rewrite the Hamiltonian in the second-quantized formalism, by defining the creation and annihilation operators through

$$n = n_\text{zpf}(a^\dagger - a), \tag{2.3}$$

$$\varphi = \varphi_\text{zpf}(a^\dagger + a), \tag{2.4}$$

where $n_\text{zpf} = (E_\text{L}/32E_\text{C})^{1/4}$ and $\varphi_\text{zpf} = (2E_\text{C}/E_\text{L})^{1/4}$ are the zero-point fluctuations of their respective variables. With this, we can finally write the Hamiltonian in the familiar quantum harmonic oscillator formulation:

$$H = \hbar\omega_\text{r}(a^\dagger a + \frac{1}{2}). \tag{2.5}$$

The eigenstates of this Hamiltonian, typically denoted as $|n\rangle$ for $n = 0, 1, 2 \ldots$, have evenly spaced energies separated by $\hbar\omega_\text{r} = \sqrt{8E_\text{L}E_\text{C}}$. This energy spacing, with $\omega^{0\to1} = \omega^{1\to2} = \omega^{2\to3} = \cdots$, is characteristic of harmonic oscillators, but is unsuitable as the basis of a qubit system. In order to treat the $(|0\rangle, |1\rangle)$ subspace as a good approximation to the 2-dimensional Hilbert space required for a qubit, we need to have a transition frequency $\omega^{0\to1}$ sufficiently distinct from transition frequencies to higher states – to prevent simultaneously driving transitions to higher states while performing qubit operations. This can be done by creating an anharmonicity in the system, which is typically done through the introduction of a Josephson junction.

2.1.2 The Superconducting Qubit

The Josephson junction serves as a means of introducing nonlinearity into the LC resonator. Josephson junctions are typically constructed by separating two superconducting elements with an insulating layer (such as Al-AlOx-Al).
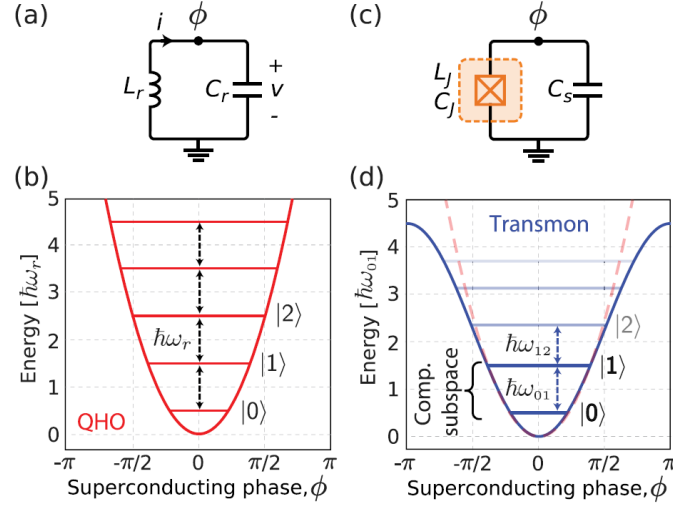
Figure 2.1: Adapted from Krantz et al. (2019) [8]. a) Diagram of a parallel LC circuit. b) Energy potential as a function of the reduced flux φ, illustrating the evenly spaced eigenenergies. c) Diagram of a Josephson junction shunted by a large capacitance, highlighting the Josephson inductance L_j and capacitance C_j. d) New energy potential (with QHO energy potential in faded red), highlighting the third-order nonlinearity for large phases, and its impact on the eigenenergies.

With a sufficiently thin insulating layer, the overlap between the Cooper pair wavefunctions in the two superconducting islands leads to almost dissipationless current flow and a nonlinear inductance.

In particular, the Josephson junction relations [9] are given as

$$I = I_c \sin \varphi, \tag{2.6}$$

$$V = \frac{\hbar}{2e}\frac{d\varphi}{dt}. \tag{2.7}$$

I_c here defines the *critical current*, the maximum current that can flow through the junction in the dissipationless regime. We can use these relations to demonstrate the I-V nonlinearity of the junction, as

$$\frac{\partial I}{\partial t} = I_c \frac{2e}{\hbar} \cos(\varphi) V.$$

This gives us the inductance as a function of φ, and the following useful set of results for junction characterisation,

$$L(\varphi) = L_J / \cos(\varphi), \tag{2.8}$$

$$L_J = \frac{\hbar}{2e I_c}, \tag{2.9}$$

$$E_J = \frac{\hbar}{2e} I_c, \tag{2.10}$$

as well as the Hamiltonian contribution of the junction itself,

$$H = -E_J \cos(\varphi).$$

In practice, due to the construction of the junction as two conducting elements separated by an insulating element, there is also a stray capacitance term. This capacitance term, however, is absorbed by the large capacitance we use to shunt the junction in our designs. The resulting system, referred to as the *transmon*, is elaborated on in Section 2.1.2.

Taking the capacitance term from Equation 2.2, we obtain the full Hamiltonian,

$$H = E_C n^2 - E_J \cos(\varphi). \tag{2.11}$$

The charging energy is now redefined as $E_C = e^2/2C_\Sigma$, where $C_\Sigma = C + C_J \gg C_J$ represents the total capacitance. We can establish that this is an anharmonic oscillator by considering the power series expansion of the junction term (for small φ) and then returning to the second quantisation formalism, to fourth order [8],

$$H = \hbar\omega_q a^\dagger a - \frac{\alpha}{2} a^\dagger a^\dagger aa, \tag{2.12}$$

where we reuse the creation and annihilation operators of Equations 2.3 and 2.4.

Thus, we finally arrive at a system where the lowest level energy states can be used as a qubit. We can also obtain the properties that characterise this system in isolation,

$$\omega_q = \omega^{0 \to 1} = (\sqrt{8E_C E_J} - E_C)/\hbar, \tag{2.13}$$

$$\alpha = \omega^{0 \to 1} - \omega^{1 \to 2} \approx E_C/\hbar. \tag{2.14}$$

Here, α is the *anharmonicity*, and is typically positive by this convention.

The Transmon Qubit

For the purpose of illustrating the role of the Josephson junction in adding anharmonicity to our system, we have omitted a term in Equation 2.11 – that is, the *offset charge*. In reality, the equation looks more like this:

$$H = E_C(n - n_g)^2 - E_J \cos(\varphi). \tag{2.15}$$

The offset charge term n_g is defined by external DC bias, and accounts for the the decoherence mechanism of charge noise. This mechanism scales with E_C; when the charging energy dominates (for $E_J/E_C < 1$), the energy eigenstates can be approximated by the charge states themselves, but the energies of these charge states are dependent on n_g, and so are strongly affected by
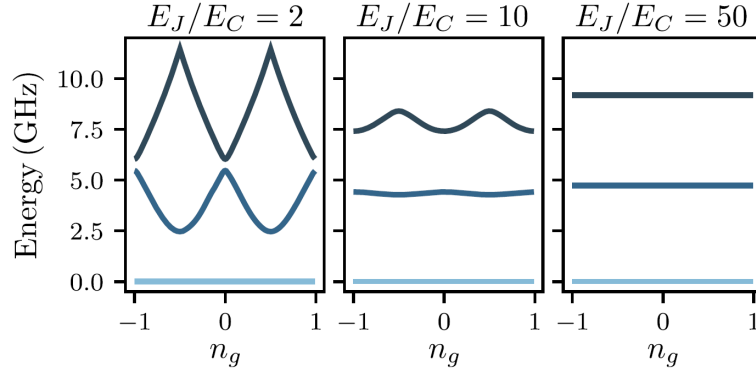
Figure 2.2: Adapted from Blais et al. (2021) [7]. These graphs illustrate the energies of the first three eigenstates as a function of n_g, for different ratios of E_J/E_C. As we can see, the energies fluctuate less with larger values of E_J/E_C, but the spacing between levels becomes more even.

fluctuations in external bias. As the Josephson energy begins to dominate, the energy eigenstates become less and less sensitive to charge noise, but at the cost of reduced anharmonicity, as illustrated in Figure 2.2.

The transmon regime is defined primarily by the relationship $E_J \gg E_C$ (more specifically, $E_J/E_C > 50$). For qubit frequencies in the 4–8 GHz range, we often work with anharmonicities in the range of 100–300 MHz, which give us optimal coherence times. The transmon offers an additional advantage for our setup – working with large capacitances and electric fields allows us to use piezoelectric materials to couple the qubit to mechanical systems.

2.2 The Coplanar Waveguide Resonator

While the anharmonicity of the transmon qubit is essential for the creation of a qubit system, harmonic oscillators still play a vital role in system control and readout protocols. With planar architectures, the primary means of creating such oscillators is using the *coplanar waveguide resonator*.

A coplanar waveguide resonator (CPW resonator, sometimes referred to in this text as a CPW for brevity), as illustrated in Figure 2.3, consists of a center conductor separated from a coplanar ground of the same material and thickness. The ends of this conductor can be either open (as in the figure, separated by a capacitance to ground) or shorted (directly connected to ground); these ends impose boundary conditions on the electric field, leading to the formation of discretised harmonic modes in the system [10, 7]. Throughout this project, we work with CPWs with both ends open – typically referred to as $\lambda/2$ resonators – and so it can be assumed that we are referring to this configuration for the rest of this thesis.
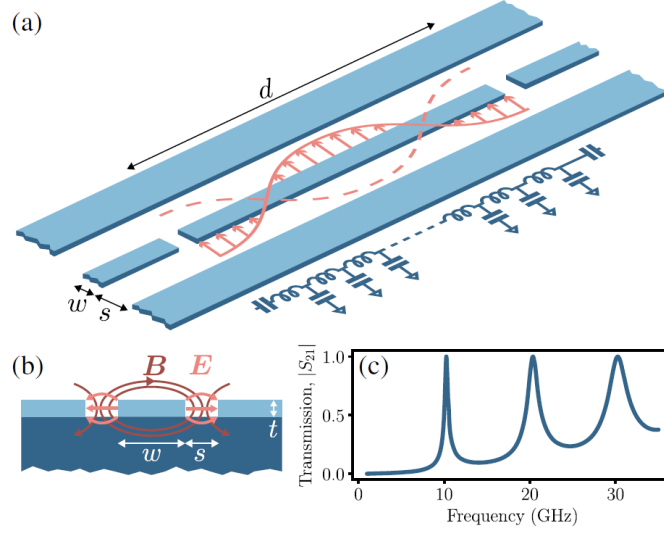
Figure 2.3: Adapted from Blais et al. (2021) [7]. a) Layout of an end-coupled coplanar waveguide resonator, of length d, width w and ground plane separation s. b) Cross section of the center conductor, illustrating the electric and magnetic field distributions through the metal and substrate. c) Transmission spectrum, illustrating the first three resonances at 10, 20 and 30 GHz.
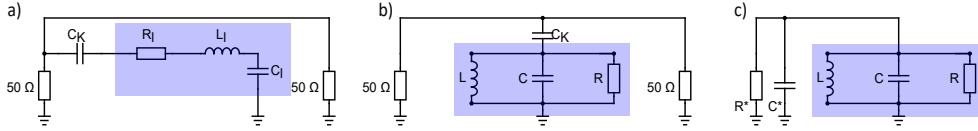
2.2.1 The CPW Resonator in Isolation

Figure 2.4: Alternate representations of the configuration used in this project. a) Distributed circuit representation of a CPW capacitively side-coupled, indicating the resistance R_l, capacitance C_l, and inductance L_l per unit length, as well as the load resistance of $Z_0 = 50\Omega$ and coupling capacitance C_K. b) A parallel RLC representation of the same CPW, with net parameters R, L, C derived from the distributed circuit representation. c) The input-output connections rewritten with a parallel representation, replacing the 50 Ω load and C_K with R^* and C^*.

Close to resonance, the behaviour of the CPW resonator can be modelled as a parallel RLC circuit [10], as seen in Figure 2.4. We primarily work with the fundamental mode, and can extract the frequency and quality factor of this mode by working with the lumped element representation. It is useful to first consider the system in isolation (in the absence of input/output lines and contributions) – in this ideal case, the *fundamental frequency* is given by,

$$f_0 = \frac{c}{\sqrt{\varepsilon_\mathrm{eff}}} \frac{1}{2l}, \tag{2.16}$$

$$v_\mathrm{ph} = \frac{c}{\sqrt{\varepsilon_\mathrm{eff}}} = \frac{1}{L_\mathrm{l} C_\mathrm{l}}, \tag{2.17}$$

where v_{ph} is the phase velocity, and ε_{eff} is the relative permittivity of the CPW line itself. These are defined by the geometry of the system and the relative permittivity of the substrate and oxide layers. Similarly, C_l and L_l are functions of the geometry of the system, and influence both the phase velocity and the *characteristic impedance* $Z_0 = \sqrt{L_l/C_l}$.

The simplest way to tune the fundamental frequency of a CPW resonator is to exploit the reciprocal relationship in Equation 2.16, and vary the length of the resonator. We also want to tune the quality factor – which, in the absence of external mechanisms, is given solely by the *internal quality factor* Q_{int}. Q_{int} represents intrinsic loss mechanisms (such as surface/bulk dielectric loss), contributions which are also incorporated in the net resistance R.

We write both (angular) frequency and quality factor as functions of the RLC representation parameters,

$$\omega_0 = \frac{1}{\sqrt{LC}}, \tag{2.18}$$

$$Q_{int} = \frac{\pi R}{2Z_0}. \tag{2.19}$$

2.2.2 Input-Output Coupling

Both the frequency and quality factor are affected by the external loading of the system [10]. The fundamental frequency is shifted by the additional shunt capacitance introduced through the transmission line, as illustrated in Figure 2.4c. The shifted frequency is given as,

$$\omega_0^* = \frac{1}{\sqrt{L(C + 2C^*)}}. \tag{2.20}$$

In the regime of small capacitive coupling (in particular, $\omega_0 C_K Z_0 \ll 1$), we can conclude that $C + 2C^* \approx C$, and so the impact on the fundamental frequency is minimal and can be neglected.

The impact on the quality factor is much more significant. The internal quality factor remains the same, but now the input-output coupling allows the resonator to decay into the transmission line, providing a new loss channel. This can be summarised through the *external quality factor* [10],

$$Q_{ext} = \omega_0 R^* C \approx \frac{2C}{\omega_0 Z_0 C_K^2} \propto C_K^{-2}. \tag{2.21}$$

Q_{int} and Q_{ext} combine into the net quality factor $Q = (Q_{int}^{-1} + Q_{ext}^{-1})^{-1}$, and the behaviour of this net quality factor can be deduced from Equation 2.21. Low C_K gives us an *undercoupled* system (defined by $Q_{ext} \gg Q_{int}$), and the net quality factor is limited by the internal losses. Inversely, a high C_K gives us an *overcoupled* system ($Q_{ext} \ll Q_{int}$), and the net quality factor drops rapidly with increasing C_K.

2.2.3 Measurement and Tradeoffs

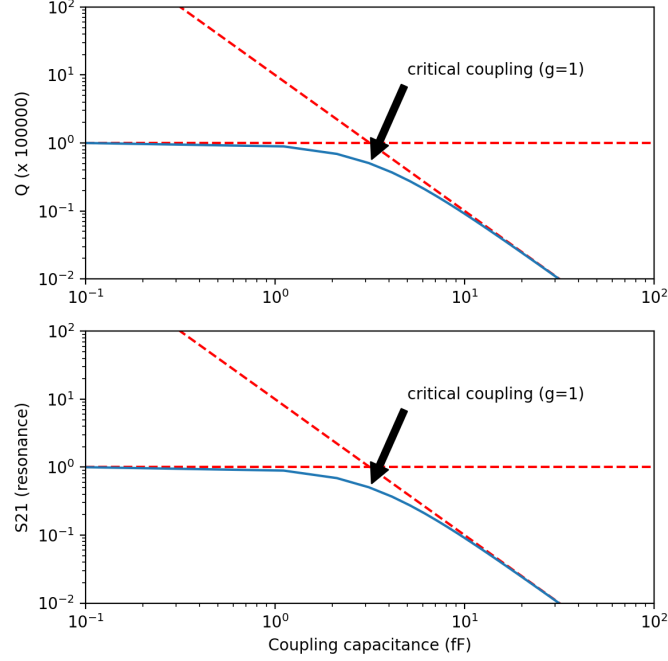**Figure 2.5:** Plotting net quality factor Q and transmission on resonance S_{21}^{res} as a function of the coupling capacitance C_K. We see that the optimal tradeoff occurs at critical coupling.

However, the net quality factor is not the only factor to consider when designing our CPW resonator and its connections. We must also consider the measurement scheme used, and the requirements imposed by this scheme.

For non-destructive measurement schemes such as dispersive shift readout (elaborated in Section 2.3.2), we extract the resonance frequency from the transmission spectrum – that is, we provide an input signal at different frequencies, measure the output signal, and compare amplitudes and phases. Far from resonance, for the side-coupling scheme in Figure 2.4, the resonator has no impact on the transmission; close to resonance, the input signal drives the resonator mode and decays through the resonator, resulting in a drop in transmission. The greater the drop in transmission, the more clearly we can resolve our resonance frequency.

The impact of the resonator can be summarised in the *transmission function on resonance* S_{21}^{res} [11],

$$S_{21}^{\text{res}} = 1 - \frac{Q_{\text{int}}}{Q_{\text{int}} + Q_{\text{ext}}}. \tag{2.22}$$

As intuited earlier, this describes a deviation from unity at resonance that

10

scales with decreasing Q_{ext}. We can further describe both S_{21}^{res} and Q through the use of the *coupling coefficient* $g' = Q_{int}/Q_{ext}$, giving us

$$Q = \frac{Q_{int}}{1 + g'},$$

$$S_{21}^{res} = \frac{1}{1 + g'},$$

and as demonstrated in Figure 2.5, they show the same behaviour. Unfortunately, while we wish to *maximise Q* (and thus minimise resonator linewidth), we also wish to *minimise S_{21}^{res}* in order to maximise resonance amplitude, giving rise to competing criteria.

Where we find our compromise depends on the task being performed. For the purpose of resonator measurements (obtaining internal quality factors and resonance frequencies, for tasks such as calibration), we benefit most from operating at *critical coupling* ($g' = 1$). However, for resonators being tuned for qubit readout, we typically favour the *overcoupled regime* ($g' \approx 10$), where fast readout is a bigger concern than high resonator quality factors – and where other methods, such as Purcell filters, can be introduced instead.

2.3 Qubit-Resonator Interactions

The main interest in having a resonator (or any electromagnetic QHO) coupled to the qubit is in exploiting their interaction to perform what is called *dispersive shift readout* – a non-destructive measurement scheme that exploits the dependence of the resonator frequency on the qubit state. In addition, the resonator can be used as a medium to deliver an external drive to the qubit, in order to tune the qubit frequency using the *AC Stark shift*.

2.3.1 The Jaynes-Cummings Hamiltonian

To understand the origin of these behaviours, it is first helpful to understand the behaviour of the coupled qubit-resonator system as a whole. The combined system is described by the following Hamiltonian [7],

$$H = \left[\hbar\omega_r a^\dagger a\right] + \left[\hbar\omega_q b^\dagger b - \frac{\alpha}{2}b^\dagger b^\dagger bb\right] + \left[\hbar g(a^\dagger b + ab^\dagger)\right]. \qquad (2.23)$$

This equation assumes that it is sufficient to consider the transmon's interaction with the closest resonator mode, and that the coupling between these modes, given by g, is real. The first two terms can be recognised from Equations 2.5 and 2.12 (dropping the constant term), and describe the resonator and qubit respectively. The third term describes the interaction between
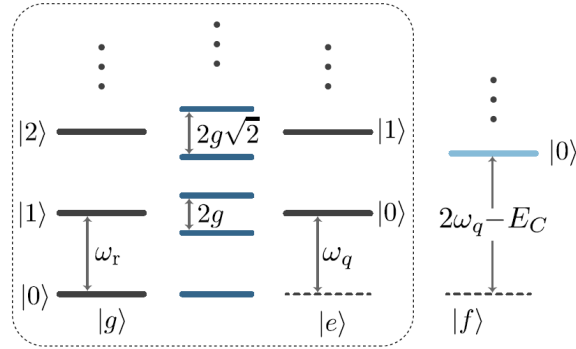
Figure 2.6: Adapted from Blais et al. (2021) [7]. Box: Illustrating the dressed states when the qubit and resonator are on resonance. The degeneracy of the bare states is broken by the interaction term, leading to the formation of 'doublets' with same total occupation but different individual occupation numbers, separated by energies proportional to the interaction strength g. Outside: The third energy eigenstate of the transmon, which is neglected in the JC Hamiltonian, but has contributions to dressed states that are nearby in energy.

the resonator and qubit, typically mediated by a capacitive coupling, and is derived using the rotating wave approximation ($|\omega_r - \omega_q| \ll \omega_r + \omega_q$).

This Hamiltonian can be slightly simplified when considering the behaviour of the system as a qubit. We truncate the transmon Hamiltonian, considering only the ground and first excited state (the qubit states) subspace, arriving at the famous Jaynes-Cummings Hamiltonian [12, 7],

$$H_{JC} = \hbar\omega_r a^\dagger a + \frac{\hbar\omega_q}{2}\sigma_z + \hbar g(a^\dagger\sigma_- + a\sigma_+). \tag{2.24}$$

The second term still describes the transmon, but now as a two-state system, with σ_- (σ_+) replacing the qubit annihilation (creation) operator.

The Jaynes-Cummings Hamiltonian is exactly solvable, and illustrates the formation of dressed states from the bare states associated with the qubit and resonator. In the case of resonance ($\omega_q = \omega_r$), the dressed states are pictured in Figure 2.6. The coupling term has the effect of breaking the degeneracy of the bare states; this behaviour manifests during qubit frequency sweeps as an 'avoided crossing', which we can use to measure resonator modes.

It is also worth looking at the parameters that influence the *qubit-CPW coupling g*, which is given by [7],

$$g = \omega_r \frac{C_g}{C_\Sigma} \left(\frac{E_J}{2E_C}\right)^{1/4} \sqrt{\frac{\pi Z_0}{R_K}}, \tag{2.25}$$

where C_Σ and C_g are the total qubit capacitance and qubit-CPW coupling capacitance respectively, and $R_K = h/e^2$ is the resistance quantum. As expected, we see a linear relationship between g and C_g, but several additional relationships between qubit/resonator properties and g, the effects of which are discussed in Section 3.3.2.
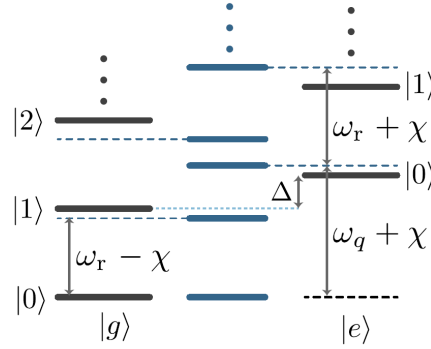
2.3.2 Dispersive Shift Readout

Figure 2.7: Adapted from Blais et al. (2021) [7]. In the dispersive regime, the dressed states remain close approximations to the bare states, but their energies are shifted in opposite directions by the transmon. As a result, the energy of the $|0\rangle \to |1\rangle$ transition depends on the qubit state.

Unfortunately, the strongly resonant regime – spanned by states that are superpositions of equal total occupation – is not particularly useful for quantum computing operations that rely on the qubit bare states. Instead, we work in what is known as the *dispersive regime* – defined by the condition $g/\Delta \ll 1$, where $\Delta = \omega_q - \omega_r$ is the *detuning*. (It is worth noting that Δ is typically negative in this text.)

Under this condition, the two systems are only weakly interacting, and the JC Hamiltonian becomes [7]

$$H_{\text{disp}} \simeq \hbar\omega_r a^\dagger a + \frac{\hbar\omega_q}{2}\sigma_z + \frac{\hbar\chi}{2}a^\dagger a\sigma_z, \tag{2.26}$$

$$= \hbar\left(\omega_r + \frac{\chi}{2}\sigma_z\right)a^\dagger a + \frac{\hbar\omega_q}{2}\sigma_z, \tag{2.27}$$

The first term in Equation 2.27 can be read as a shift in resonator frequency based on qubit state. (In this equation, we neglect the impact of the Lamb shift on the qubit and resonator frequencies.) We can further derive the *dispersive shift* χ (typically negative in this text) [7, 5] as a function of anharmonicity, detuning and coupling strength,

$$\chi = -2\frac{g^2}{\Delta}\frac{\alpha}{\Delta - \alpha}. \tag{2.28}$$

This gives us a means of performing a quantum nondemolition measurement of the qubit state, as illustrated in Figure 2.8. When driving the resonator close to ω_r, the coherent state of the resonator becomes entangled with the qubit state, and therefore can be used as a pointer state. Consequently, a measurement of the resonator allows us to read out the qubit state – and, in the case of the qubit being in a superposition of the $|0\rangle$ and $|1\rangle$ states, causes the qubit to collapse into the measured state.
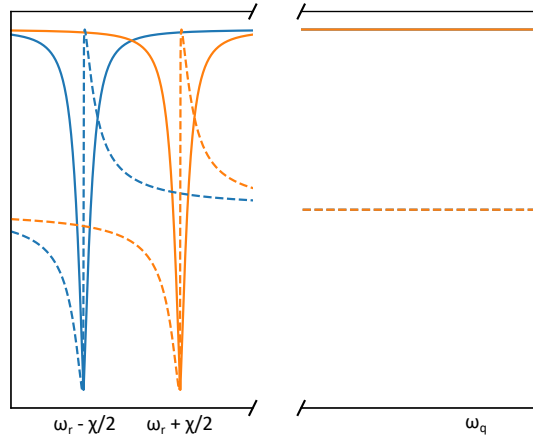

Figure 2.8: Amplitude and phase plots of the transmitted signal for a qubit in the ground state (blue) and excited state (orange). At the frequency of the qubit – far detuned from the resonator – we see that the qubit has a negligible impact on the resonator behaviour, limiting resonator-mediated decoherence processes.

Figure 2.8 also suggests a natural limitation on this measurement scheme. As visible in the figure, it is necessary that the dispersive shift to linewidth ratio χ/κ be high enough to clearly resolve the different resonance locations. This, along with the Purcell decay mechanism described in Section 2.3.4, allow us to work out the design specifications needed for this measurement scheme.

2.3.3 The AC Stark Shift

While Equation 2.26 can be read as the impact of the qubit states on the resonator, the interaction term also implies that the resonator states have an impact on the qubit. When performing measurements, we use low power drives, and so the resonator photon number $\langle a^\dagger a \rangle = \bar{n}$ is close to zero. However, by applying a pulse close to the resonator frequency, we can drive the resonator into a coherent state with higher $\bar{n}$. Reconfiguring Equation 2.26, we can see that the qubit frequency scales linearly with $\bar{n}$,

$$H = \hbar \left(\frac{\omega_q}{2} + \frac{\chi}{2} a^\dagger a \right) \sigma_z + \hbar \omega_r a^\dagger a.$$
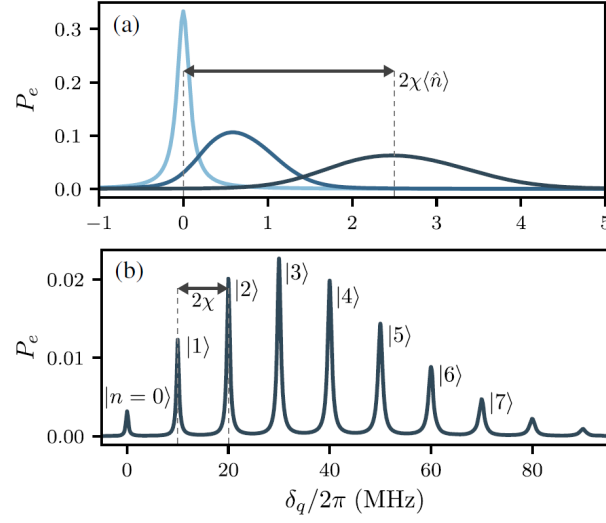
Figure 2.9: Adapted from Blais et al (2021) [7]. a) Qubit spectroscopy measurements in the weak dispersive regime for increasing Stark shift tone powers, indicating qubit frequency shift and broadening. b) Measurement in the strong dispersive regime, indicating resolved peaks for resonator Fock states.

Once again, this mechanism is limited by the value of χ. In addition, the maximum drive we can use is limited as well, as exceedingly high photon numbers [7] cause the dispersive regime approximations to break down, including the relationship between qubit frequency and drive.

2.3.4 Purcell Decay

The introduction of the resonator also adds an additional loss mechanism to the qubit. The loss mechanisms of the combined system can be described using the master equation in the dispersive regime [7, 13],

$$
\begin{aligned}
\dot{\rho}_{\text{disp}} = &- i[H_{\text{disp}}, \rho_{\text{disp}}] \\
&+ (\kappa + \kappa_\gamma)\mathcal{D}[a]\rho_{\text{disp}} + (\gamma + \gamma_\kappa)\mathcal{D}[b]\rho_{\text{disp}} \\
&+ 2\gamma_\varphi \mathcal{D}[b^\dagger b]\rho_{\text{disp}} \\
&+ \gamma_\Delta \mathcal{D}[a^\dagger b]\rho_{\text{disp}} + \gamma_\Delta \mathcal{D}[b^\dagger a]\rho_{\text{disp}}.
\end{aligned}
\tag{2.29}
$$

This equation reuses the operators of Equation 2.23, and $\mathcal{D}$ is the Lindbladian superoperator, $\mathcal{D}[L]\rho = L\rho L^\dagger - \frac{1}{2}\{L^\dagger L, \rho\}$. We recognise $\mathcal{D}[a]$ and $\mathcal{D}[b]$ as terms representing relaxation of the resonator and qubit, and $\mathcal{D}[b^\dagger b]$ as representing the dephasing of the qubit. The terms $\mathcal{D}[a^\dagger b]$ and $\mathcal{D}[b^\dagger a]$ are more subtle, representing a 'dressed dephasing' mechanism arising from noise at the detuning frequency.

We primarily concern ourselves with the qubit relaxation, and note that in addition to the bare qubit relaxation rate γ, there is an additional contribution

γ_κ. This contribution arises from the effect of the resonator's net loss rate (including intrinsic and extrinsic losses) κ, and can be understood as the dressed excited states being vulnerable to both qubit and resonator relaxation – in particular, we consider the dressed excited state $\overline{|e,0\rangle} \sim |e,0\rangle + (g/\Delta)|g,1\rangle$, which can decay through resonator relaxation to the ground state $|g,0\rangle$.

This mechanism, of the qubit relaxing through resonator decay, is called *Purcell decay*, and occurs with a rate of

$$\gamma_\kappa = \left(\frac{g}{\Delta}\right)^2 \kappa. \tag{2.30}$$

Comparing this to Equation 2.28, we see that the dispersive shift and the Purcell decay scale similarly. For this project, the maximum values of χ that can be achieved are therefore limited by the Purcell decay rate. While this mechanism can be mitigated using Purcell filters, we leave that discussion to the outlook.

2.4 Qubit-HBAR Interactions

We dedicate a small section to describing the mechanical aspect of the $\hbar$BAR, as it has a bearing on the project. As noted in Chapter 1, the qubit is coupled to a bulk acoustic resonator through the use of a piezoelectric dome and a qubit antenna. The same principles of the cQED dispersive model can be applied to the case of a coupled qubit and HBAR [5], with the resulting Hamiltonian (neglecting the resonator for simplicity) being,

$$H = \hbar \left(\frac{\omega_\mathrm{q}}{2} + \frac{\chi}{2}c^\dagger c\right)\sigma_\mathrm{z} + \hbar\omega_\mathrm{m}c^\dagger c,$$

which we recognise, apart from the phonon annihilation and creation operators c and $c^\dagger$ and the mode frequency ω_m, as identical to Equation 2.26 – provided that we can make the same assumption $\Delta \gg g$. This parallel gives us some basic insights.

Firstly, the HBAR demonstrates a much more dense mode structure than the microwave resonators of circuit QED, with a longitudinal FSR of ~ 12 MHz and a spacing between different Laguerre-Gaussian mode numbers of ~ 1 MHz. Much like in the cQED dispersive model, we operate with the assumption of coupling to a single mode (the LG-00 fundamental mode), which limits our *qubit-HBAR coupling* $g_\mathrm{an} \leq 1$ MHz.

Secondly, the same mechanisms of dispersive shift and Purcell decay can be used to understand the limitations of this system, and particularly the restrictions placed on g_an. A high coupling provides a larger dispersive shift, which is useful for measurement and operation schemes, but also increases
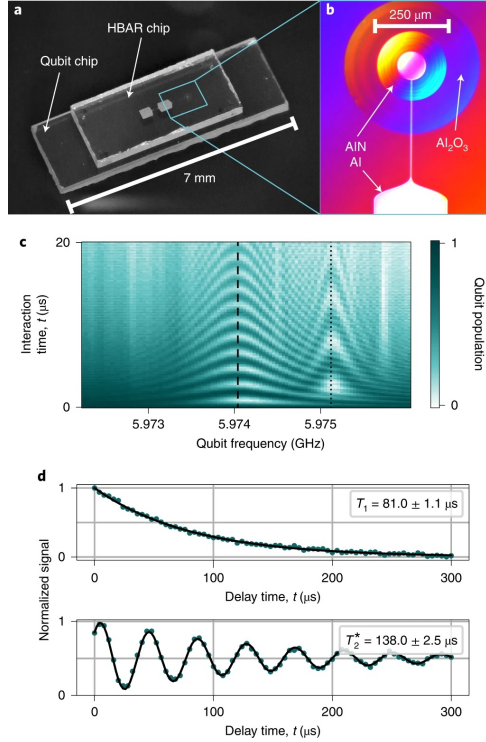
Figure 2.10: Adapted from von Lüpke et al. (2022) [5]. a) A photograph of the $\hbar$BAR setup. b) An image of the qubit antenna and the piezoelectric dome on the HBAR. The largest circle depicts a shallower sapphire dome formed during the etching process. c) Rabi oscillations between the qubit and phonon modes, highlighting the LG-00 (dashed) and LG-10 (dotted) modes. d) Coherence times of the LG-00 phonon mode.

the impact of loss through the HBAR. Unfortunately, our coupling mechanism (the piezoelectric dome) also introduces a number of loss mechanisms, such as diffraction loss and multimode coupling. These exact mechanisms remain to be fully studied, but they limit our range of g_{an} further still.

2.5 System Constraints

The results of this chapter can be summarised by reviewing the constraints that cQED theory imposes on our system, which are as follows:

- **Anharmonicity vs charge noise:** Operating with the transmon design offers us many advantages, including insensitivity to charge noise. However, the resulting anharmonicity is quite low, resulting in a poorer approximation to the two-level system required for a qubit.

- **Dispersive shift vs Purcell decay:** A large dispersive shift allows for faster readout, but leads to greater qubit relaxation through the resonator, ultimately limiting our coherence times.

- **Phonon dispersive shift vs HBAR loss mechanisms:** Similarly, a large qubit-HBAR coupling leads to large dispersive shifts, but also leads to loss through the HBAR, reducing our coherence times.

From these system constraints, we can devise our design specifications, which are discussed in the next chapter.

Chapter 3

Chip Design

3.1 Design Overview
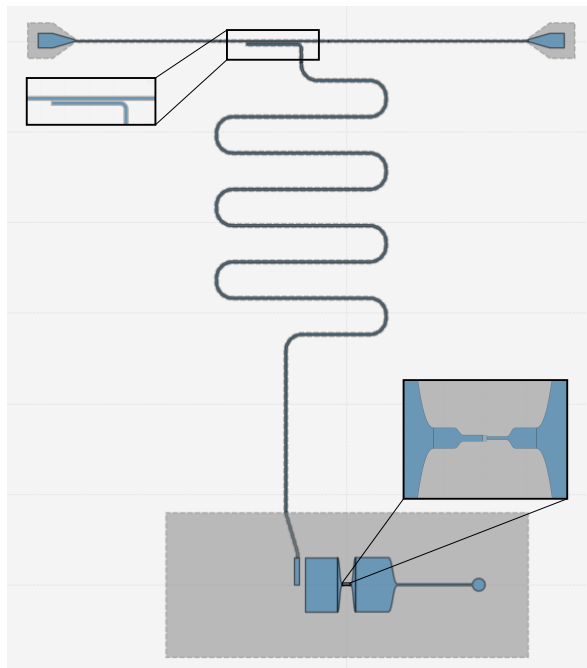
Figure 3.1: A design of a single qubit coupled to a transmission line, taken from the Qiskit Metal GUI. *Inset:* The junction and adjacent funnels. The funnels serve to avoid sharp corners (as in the default Qiskit Metal design), which lead to high electric fields and high dielectric losses.

The basic setup we use is pictured in Figure 3.1. The design has three major components:

- A transmission line, with launchers on either end for wirebonding.

- A modified *pocket transmon*, composed of two large pads separated by a junction, placed in a large pocket separating these components from the ground plane. We add an antenna to one of the transmon pads (consisting of a long thin segment leading to a circular conductor), which provides the coupling to the HBAR.

- A CPW resonator, capacitively coupled to the transmission line using a straight segment running parallel to it, and capacitively coupled to the qubit using a larger connector pad.

The fourth major component in design and simulation is the mechanical resonator this system is coupled to – the HBAR – and while this component is not tuned as part of this project, it must be incorporated in simulations. This component, which is visible in Figure 3.2, is comprised of the sapphire block itself, and a piezoelectric dome placed directly over the qubit antenna. This layout is better described in Section 3.2.3.

3.1.1 Design Specifications

As explained in the previous chapter, our chip design must conform to a number of requirements for optimal performance. We finalise acceptable ranges for our design properties here in Table 3.1.

Design Specifications	Values
Qubit frequency, ω_q (GHz)	4–8
Detuning, $|\Delta|$ (GHz)	1.5–2
Anharmonicity, α (MHz)	170–200
Dispersive shift, $|\chi|$ (MHz)	2–5
Qubit-HBAR coupling, g_{an} (kHz)	100–200
External quality factor (resonator), Q_{ext}	≈ 50000

Table 3.1: Resonator and qubit design specifications. Properties that would be negative are listed as absolute values for convenience. We otherwise follow the same conventions used in Chapter 2.

As discussed in Section 2.5, we aim for design properties that satisfy our system constraints. Our dispersive shift is limited by our resonator linewidth (on the order of 100 kHz) and the Purcell decay rate (which should have a characteristic timescale of above 50 us), and our anharmonicity and qubit-HBAR coupling ranges are selected based on their observed effects on qubit coherence times. Our qubit and resonance frequencies are limited by our measurement setup, including input oscillators and amplifiers. Our external quality factor Q_{ext} is limited by the internal quality factor of our resonators, and the requirement for an overcoupled system.
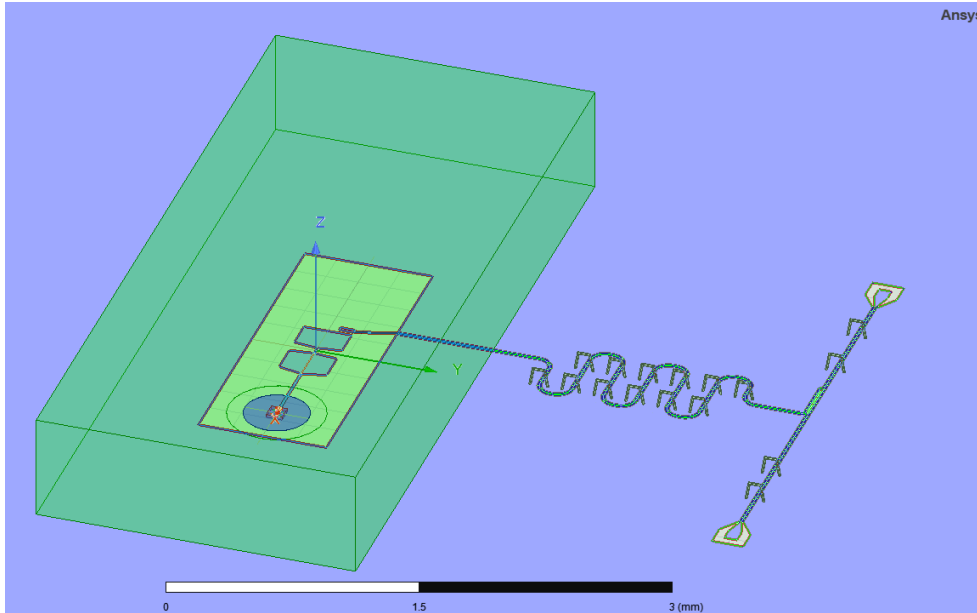
Figure 3.2: The design in Figure 3.1, recreated in Ansys for simulation. This includes the position of the HBAR, and the position of the piezoelectric dome. The airbridges are used only for simulation purposes, and are not included in the actual design.
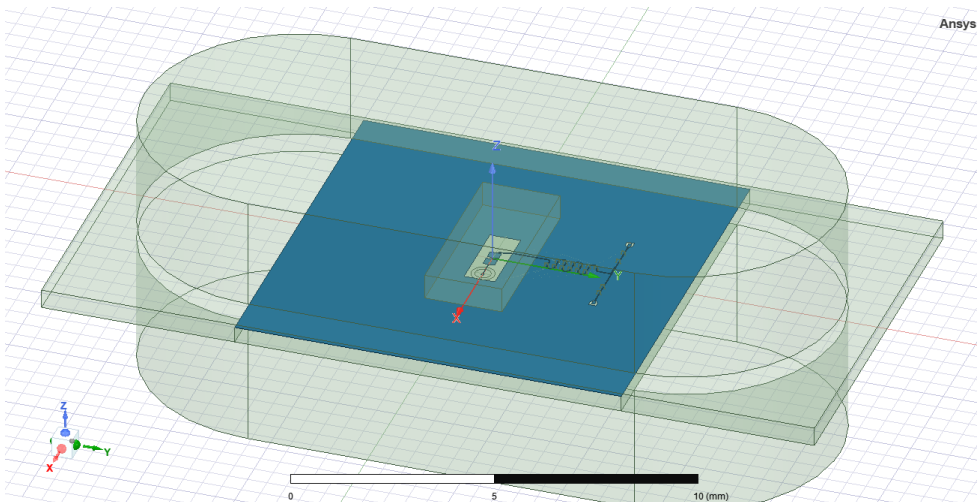

Figure 3.3: Zoomed out picture of the Ansys design, showing the full qubit chip and the cavity/sample holder. In practice, the sample holder does not have this exact shape, but it has similar dimensions.

21

There are a large number of variables that go into this design, and they can be sorted into qubit and resonator parameters. These parameters have different effects on the design properties, and understanding these impacts was a major aspect of this project. We go into these parameters and their relationships with the properties above in Section 3.3.

3.2 Simulation Methods

We use two main software packages to create designs in this project. *Qiskit Metal* [14] is an open-source framework that allows us to quickly design and modify qubits, resonators, and other chip components, and generate GDS files for simulation and fabrication. *Ansys HFSS* [15], a 3D electromagnetic simulation software package, allows us to perform microwave frequency simulations, extract participation ratios and electric field distributions, and ultimately calculate design parameters and tune them.

We provide a brief summary on the methods used in Ansys HFSS, starting with the underlying principle of HFSS numerical simulations and progressing to extracting qubit parameters from simulations.

3.2.1 HFSS Principles

Ansys HFSS uses a technique known as the Finite Element Method. The procedure used can be summarised as follows [15]:

1. We divide the complex 3-dimensional structure into a mesh of tetrahedrons (finite elements).

2. We define 'testing functions' W_i for each of the N tetrahedral elements. These functions work as basis functions for the electric field approximation $\bar{E}$,

$$\bar{E} = \sum_i^N x_i W_i. \tag{3.1}$$

   where x_i defines the contribution of each testing function toward the approximator.

3. We start with the wave equation, subject to materials, excitations and boundary conditions,

$$\Delta \times \left(\frac{1}{\mu_r} \Delta \times E \right) - k_0^2 \varepsilon_r E = 0, \tag{3.2}$$

   where $\mu_r = \mu/\mu_0$, $\varepsilon_r = \varepsilon/\varepsilon_0$, and $k_0^2 = \omega^2/c^2$.

Multiplying both sides of this equation by each working function, manipulating these equations, and incorporating the boundary conditions, we obtain N equations,

$$\int_V \left[(\Delta \times W_i) \cdot \frac{1}{\mu_r} \Delta \times E - k_0^2 \varepsilon_r W_i \cdot E \right] dV = \int_S (\text{boundary terms}) \mathrm{d}S.$$

Inserting Equation 3.1 back into this, we arrive at,

$$\sum_j x_j \int_V \left[(\Delta \times W_i) \cdot (\frac{1}{\mu_r} \Delta \times W_j) - k_0^2 \varepsilon_r W_i \cdot W_j \right] dV$$

$$= \int_S (\text{boundary terms}) \mathrm{d}S.$$

These N equations, along with the vector terms x_j and the boundary integrals, can be written in a matrix formulation. In particular, the previous equation becomes

$$\sum_j A_{ij} x_j = b_i, \tag{3.3}$$

which we recognise as a system of linear equations. The matrix $\mathbf{A}$ and vector $\mathbf{b}$ that arise from these equations incorporate boundary conditions, incident waves, port excitations, and voltage and current sources.

4. Solving this equation, however, only brings us to an approximate solution. The error of this solution, referred to as the *residue r*, can be given by putting the approximation back through the wave equation 3.2:

$$\Delta \times \left(\frac{1}{\mu_r} \Delta \times \bar{E} \right) - k_0^2 \varepsilon_r \bar{E} = r \tag{3.4}$$

We select the elements with the highest resides, and refine these elements by replacing them with a number of smaller elements.

5. We iterate through the previous steps, calculating a solution and refining the mesh until the convergence criteria are met, or until the maximum number of iterations – passes – have been completed.

We can exploit the principles of the Finite Element Method to optimise our simulations. In particular, we can compel the meshing algorithm to focus on certain regions of the design – in our case, the high-priority regions are the junction, which experiences the highest fields and finest features, and the antenna end, the field calculation of which is used to obtain the qubit-HBAR coupling. Ansys also allows us to generate the mesh used to solve for a given design without actually solving for the E-field, allowing us to check whether the solver accounts for all important features without wasting time and processing power.

3.2.2 Eigenmode Simulation and EPR Analysis

Ansys HFSS offers a number of solution methods, but we operate mainly with the frequency-domain eigenmode solver. This method solves Equation 3.3 in the absence of external energy sources, calculating the eigenmodes – the natural resonances – of the system given the assigned materials and surfaces. This allows us to obtain the electric field distributions for each of these modes, and allows us to estimate the unloaded quality factors of these modes. In our case, operating in the 4–8 GHz range, this gives us the qubit and fundamental resonator modes, shown in Figures 3.4 and 3.5.
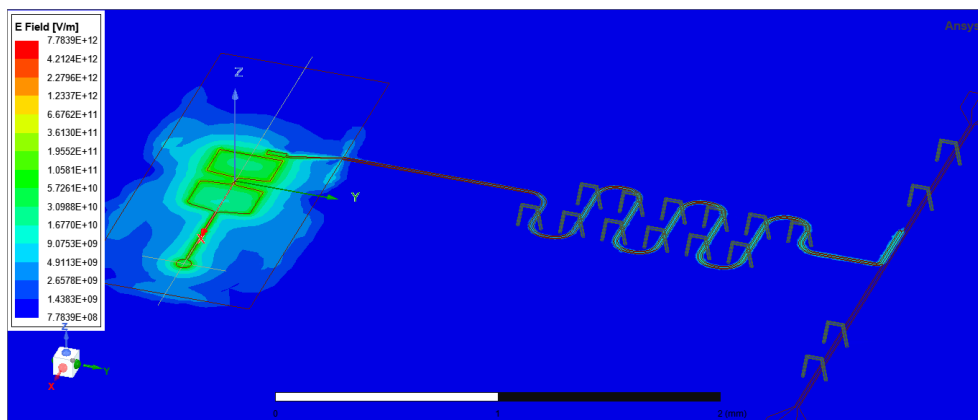

Figure 3.4: Electric field distribution of the qubit mode, on the upper face of the qubit chip. We note that the qubit acts as a dipole, with highest electric field magnitude close to the junction separating the two pads.
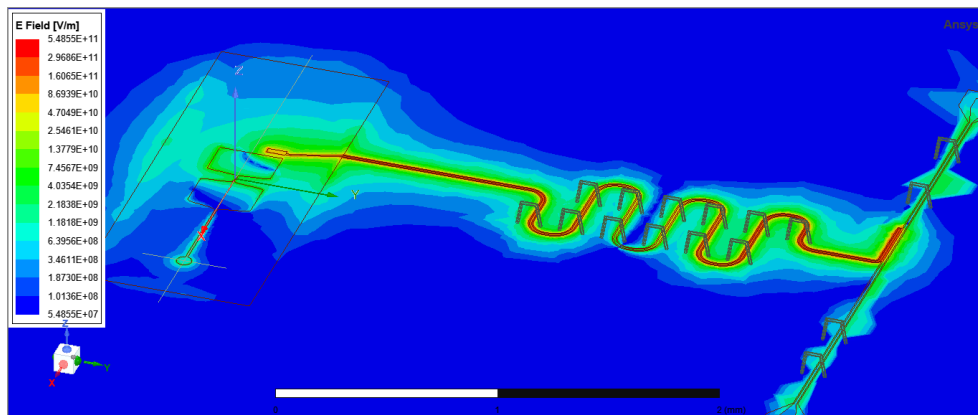

Figure 3.5: Electric field distribution of the fundamental resonator mode, on the upper face of the qubit chip. We note the high field magnitudes at either end of the resonator, and the low magnitude at the middle.

Understanding the E-field distributions for the qubit and resonator modes

also allows us to perform *Energy Participation Ratio (EPR) analysis* [16, 17]. This approach, derived from first principles, allows us to obtain the Hamiltonian of a coupled qubit and resonator system from the participation ratio of the Josephson junction, i.e. the proportion of inductive energy stored in the junction for a given mode.

Revisiting Equations 2.2, and 2.11, we can choose to write the Hamiltonian of the coupled qubit and resonator in a different formalism, defining the reduced flux operator $\varphi = 2\pi\Phi/\Phi_0$ as

$$\varphi = \varphi_r(a + a^\dagger) + \varphi_q(b + b^\dagger), \tag{3.5}$$

where φ_r (φ_q) is the quantum zero-point fluctuation associated with the resonator (qubit) mode.

This definition incorporates the contribution of every circuit component to the reduced flux (compare to Equation 2.4), resulting in the following Hamiltonian, broken up into linear and non-linear components,

$$H_{lin} = \hbar\omega_r a^\dagger a + \hbar\omega_q b^\dagger b, \tag{3.6}$$

$$H_{nl} == -\sum_{p=3}^{\infty} E_J c_p \varphi^p = -E_J \cos(\varphi) - E_J \varphi^2/2, \tag{3.7}$$

where the $\varphi^2/2$ term, being a linear contribution, is removed from H_{nl}.

From these terms, we can formally define the energy participation ratio:

$$\begin{aligned} p_m &= \frac{\text{Inductive energy stored in the junction}}{\text{Total inductive energy stored in mode } m}, \\ &= \frac{\langle\psi|E_J\varphi^2/2|\psi\rangle}{\langle\psi|H_{lin}/2|\psi\rangle}, \end{aligned} \tag{3.8}$$

where p_m represents the participation ratio in mode m (i.e. either the qubit or resonator mode). p_q and p_r can be obtained directly from simulations, but can also be used to calculate φ_r and φ_q, allowing us to fully define the Hamiltonian of a given circuit. Additionally, they can also be used to calculate the qubit anharmonicity, the induced resonator anharmonicity, and the dispersive shift,

$$\alpha_q = p_q^2 \frac{\hbar\omega_q^2}{8E_J}, \tag{3.9}$$

$$\alpha_r = p_r^2 \frac{\hbar\omega_r^2}{8E_J}, \tag{3.10}$$

$$\chi = p_q p_r \frac{\hbar\omega_q\omega_r}{4E_J}. \tag{3.11}$$

From χ and from the mode frequencies given by Ansys' eigenmode solver, we can derive the detuning Δ and thus the qubit-CPW coupling g.

3.2.3 HFSS Design

When creating a design in Ansys, there are two main types of components to consider: 2D surfaces (which can be sheets, or faces of 3D objects) and 3D solids. Solids are typically useful for representing bulk materials, such as the HBAR or qubit chip, and account for properties such as material permittivity and bulk dielectric loss. Surfaces, in contrast, are useful for representing thin films, such as ground plane conductors – and, of course, Josephson junctions. We note that we work mostly with lossless simulations, and do not compute surface/bulk loss rates; for work in this direction, we recommend looking at Jonathan Knoll's codes [18].

The main 3D objects, with appropriate materials, used in this project are:

- The qubit substrate, composed of silicon, with dimensions of 10 mm x 10 mm x 0.42 mm.

- The HBAR substrate, composed of sapphire, described as the union of a cuboid with the dimensions of the HBAR (2 mm x 4.5 mm x 0.66 mm) and the cylindrical etch feature that arises from the creation of the piezoelectric dome [4], with radius 300 um and height 0.7 um. This chip is placed at a height of 1.85 um over the qubit chip (measured from chip surface to chip surface).

- The piezoelectric dome, composed of aluminum nitride, described as a cylinder with radius 200 um and height 0.65 um.

- The sample holder, which can be approximated either as a cuboid of vaccuum or a cavity (illustrated in Figure 3.3) with dimensions of 10 mm x 10 mm x 6 mm.

- The airbridges (visible in Figure 3.2), defined as perfect conductors. These are necessary for accurate simulation of the electric fields, but are not used in the actual chip.

The main 2D objects, with appropriate boundary definitions, are:

- The ground plane, qubit pads, CPW central conductor, and transmission line central conductor – which are all defined as perfectly conductive surfaces.

- The Josephson junction, defined as a *lumped element* with zero resistance, zero capacitance, inductance L_J, and current flow line in the direction of the antenna.

- The external faces (not internal faces) of the cavity/sample holder, modelled as perfectly conductive. (The 3D object of the sample holder describes the vacuum contained within the physical sample holder, and so its external faces correspond to the internal faces of the physical

sample holder — whereas the internal faces of the 3D object are in contact with the objects within.)

3.3 Design Tuning

3.3.1 Qubit Parameters

Most of the tunable parameters arise from the qubit design, so we begin with this. We build on the work in Knoll (2022) [18].
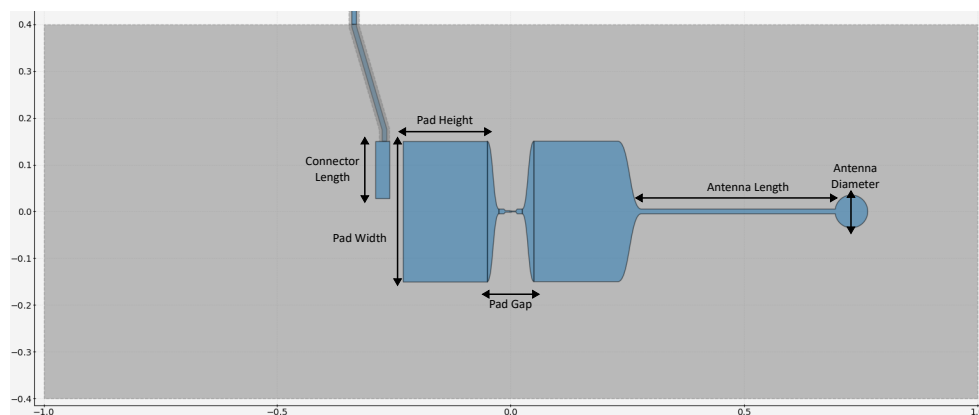

Figure 3.6: A close-up on the qubit design, with the main variables highlighted by arrows. The scale is in millimeters. For the pad width and pad height, we use the parameter names as they are in Qiskit Metal to avoid confusion.

Each parameter has different effects on the qubit properties, and these can be summarised as follows.

Qubit pad width and height

While we have the option of assigning different dimensions to each of the pads, we elect to keep them the same for the purposes of this design. We can observe the general effects of these parameters in Figures 3.7 and 3.8:

- As expected, increasing the pad width or height increases the capacitance of the qubit, decreasing E_C and thus the qubit frequency and anharmonicity.

- Increasing the pad width or height also reduces the qubit-CPW coupling g. We attribute this to a reduced overlap between the qubit and cavity mode electric fields, leading to reduced coupling.

- The pad widths of the left and right pads (and, similarly, the pad heights) have competing effects on g_{an} [18], resulting in weak trends. The general intuition is that the dimensions of these pads shape the

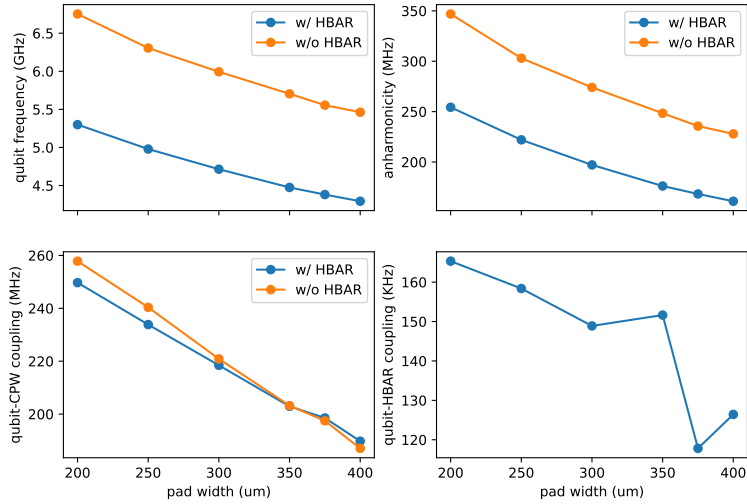**Figure 3.7:** Sweeping qubit pad width and observing its effects on qubit frequency ω_q, anharmonicity α, qubit-CPW coupling g, and qubit-HBAR coupling g_{an}. We also observe the effects of the HBAR on ω_q, α and g by performing simulations with and without the HBAR (and piezoelectric dome) present. We keep pad height constant at 180 um.
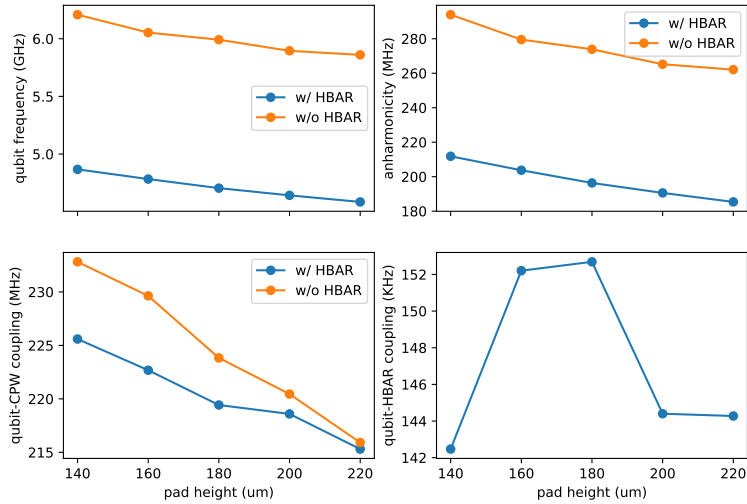

Figure 3.8: Sweeping qubit pad height and observing the effects on ω_q, α, g, and g_{an}. We also perform simulations without the HBAR present. We keep pad width constant at 300 um, and modify the antenna length so that the antenna end does not move across the sweep.

resulting dipole, and a larger left pad or smaller right pad increases the participation of the antenna as a capacitive element, thus increasing electric field strength and coupling at the antenna.

Qubit pad gap

The pad gap also influences qubit parameters through the capacitance, and its effects can be seen in Figure 3.9.

- Increasing the pad gap decreases the qubit capacitance, and thus increases the qubit frequency and anharmonicity, as expected.

- Increasing the pad gap also increases the qubit-CPW coupling. We attribute this to the creation of a less-confined qubit mode, which results in increased overlap with the resonator mode.

- Increasing the pad gap does not result in a clear trend g_{an}. We attribute this to the competing effects of decreasing field magnitude (due to the decrease in capacitance) and increasingly optimal field distribution from the longer dipole.

There is an additional factor to consider when altering the pad gap. A small pad gap results in high E-field magnitudes, which – while useful for our qubit parameters – results in high dielectric loss through the substrate (and surface). Consequently, we limit ourselves to a minimum pad gap for this project, and expect to revisit this minimum following measurements of qubit coherence times.

Josephson inductance

The Josephson inductance (or junction inductance) L_J determines E_J and therefore the qubit properties. In reality, it is determined by the dimensions of the junction; in Ansys, however, we provide it as a parameter directly to the lumped element junction, and keep the junction dimensions constant.

We can see the effect of changing the Josephson inductance in Figure 3.10.

- Changing L_J changes E_J, with predictable effects on the qubit frequency – as well as smaller effects on the anharmonicity, which still follows the rule of thumb of $\alpha \approx E_C$.

- Changing L_J also has an effect on the qubit-HBAR and qubit-CPW couplings. We interpret this as the effect of the increasing inductive energy of the system – which, through energy conservation, reduces the capacitive energy of the system, and reduces the impact of capacitance-mediated couplings such as g and g_{an}. This is in line with what we expect from Equation 2.25.
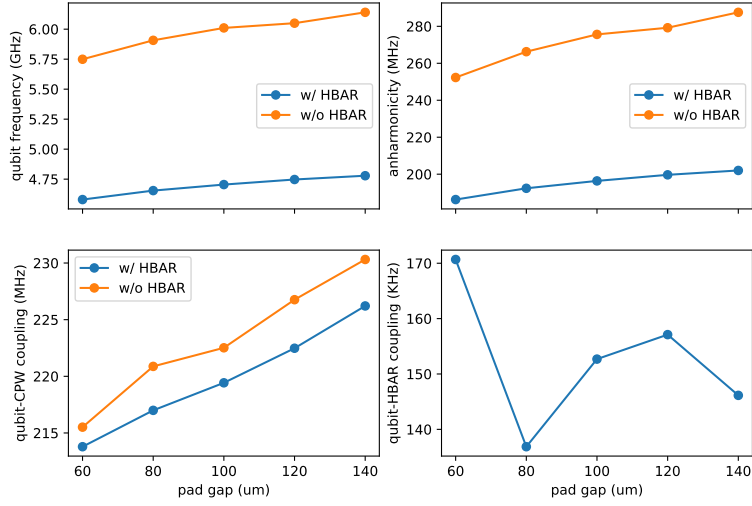
29

Figure 3.9: Sweeping qubit pad gap and observing the effects on $\omega_{\mathrm{q}}, \alpha, g$, and g_{an}. We also perform simulations without the HBAR present. We keep pad height and width constant, and modify the antenna length such that the antenna end does not move across the sweep.
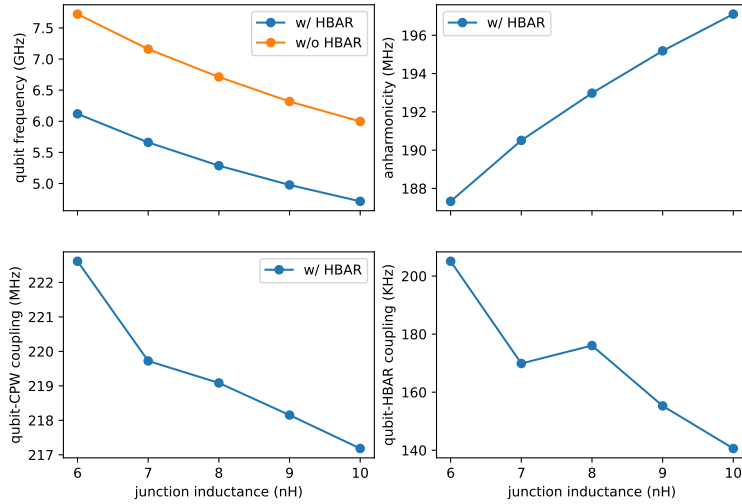
Figure 3.10: Sweeping junction inductance and observing the effects on $\omega_{\mathrm{q}}, \alpha, g$, and g_{an}. We also perform eigenmode simulations without the HBAR present, and provide the qubit frequencies in the absence of the HBAR. We keep the qubit and resonator geometry constant across the sweep.

We note that simulating the junction inductance for the design without an HBAR proved difficult in the case of lower inductances. The eigenmode analysis was unaffected, so we trust the values of mode frequency given by Ansys in these simulations; however, the EPR analysis fails to converge as the difference between inductive and capacitive energy increases, leading to untrustworthy values and trends in anharmonicity and dispersive shift. We explored alternate solutions, including the Lumped Oscillator Model analysis [14, 17]; we found that the LOM analysis showed more reasonable trends and values, but consistently underestimated capacitances between circuit components, such as the qubit pads.

Other parameters

- *Antenna length:* In this scheme, the antenna length has a small effect on the qubit properties, but influences g_{an} much more significantly. For short antenna lengths (below a certain threshold [18]), the qubit pads have a larger impact on the field passing through the piezoelectric element, leading to loss of perpendicularity and weaker coupling to the longitudinal mode. For long antenna lengths, increasing the length further reduces the electric field overlap with the piezoelectric element, decreasing g_{an}.

- *Antenna diameter:* The antenna radius determines the coupling to the phonon modes, and is controlled by a number of parameters, including the radius of curvature of the piezoelectric dome. We avoid tuning this parameter, as the domain of this project does not extend to tuning the properties of the HBAR.

Finally, there is the *connector length*, which is best viewed from the perspective of the resonator.

3.3.2 Resonator Parameters

The resonator variables govern the properties of the resonator itself (as discussed in Section 2.2). They can be summarised as follows.

Resonator length

The effects of changing the *resonator length* l_{res} can be seen in Figure 3.12. The resonator length directly affects the resonator frequency, as expected from Equation 2.16. In addition, the resonator length also has a relationship with the qubit-resonator coupling strength g, which is justified by Equation 2.25. This can be understood in terms of the electric field: a shorter resonator leads to a larger overlap of the resonator mode E-field with the qubit, leading to higher g.
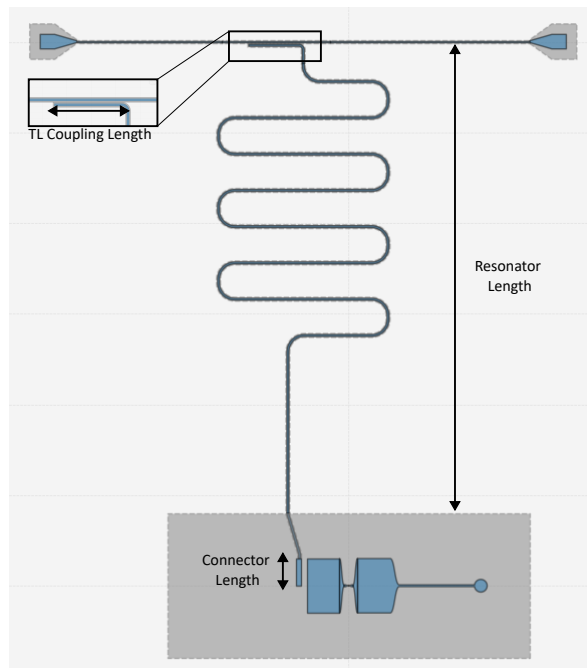
31

Figure 3.11: Illustrating the main resonator variables for the design in Figure 3.1.

Connector length

The *connector length l_{con}* influences the capacitive coupling between the resonator and the qubit, thus affecting g in a much more direct fashion, as can be seen in Figure 3.13. The connector length also has a subtle, but generally negligible effect on the resonator frequency, as expected: increasing the connector length also increases the net length of the resonator.

Other parameters

- *TL coupling length:* The length of the segment parallel to the transmission line controls the capacitive coupling to the TL, which controls Q_{ext} and S_{21}^{res}, as discussed in Section 2.2.3. We set this parameter based on experimental data discussed in Section 4.2.2.

- *CPW width and gap:* The geometry of the center conductor also possesses tunable parameters, as seen in Figure 2.3. However, these parameters affect other properties of the resonator, such as the characteristic impedance, which we would rather not change. As such, we leave these parameters intact.

Figure 3.12: Sweeping the resonator length and observing the effects on frequency and qubit-CPW coupling. We also plot these parameters in the absence of the HBAR.

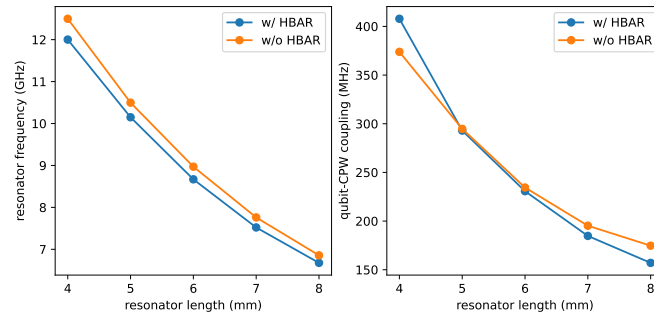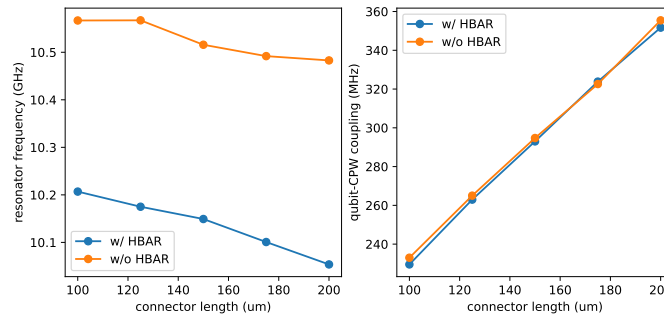**Figure 3.13:** Sweeping the connector length and observing the effects on frequency and qubit-CPW coupling. We also plot these parameters in the absence of the HBAR.
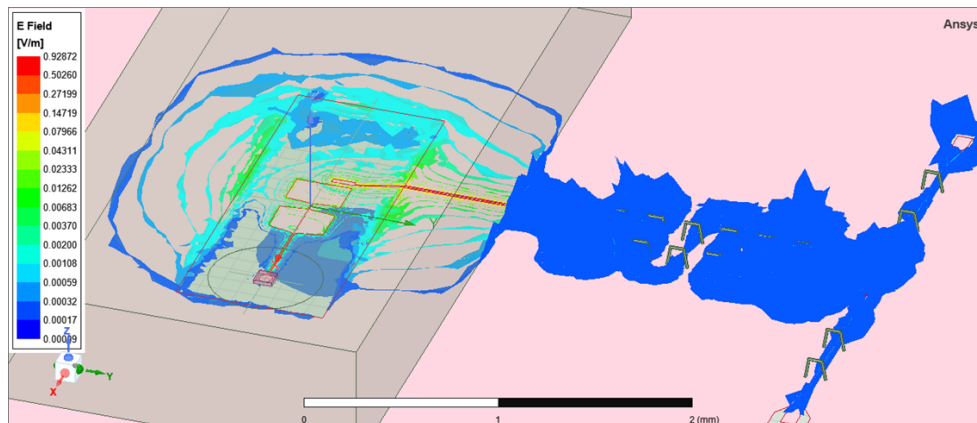
Figure 3.14: The electric field distribution in 3D space (illustrated using field magnitude isosurfaces) of the resonator mode (compare to Figure 3.5). We see that the resonator mode is spread out over the qubit due to the interaction with the HBAR. We can clearly see the boundary of the HBAR (transparent) from the 3D field distribution. The light pink surface is the perfect conductor surface of the ground plane and the qubit/CPW components.

3.3.3 HBAR Contributions

One of the main challenges of this project was in accounting for the impact of the HBAR on the qubit and resonator properties. The naive approach of attempting to iterate directly through HBAR simulations proved impractical. Firstly, Qiskit Metal did not easily allow for the creation of 3D objects or the rendering of chip designs into pre-existing projects. Secondly, simulations including the HBAR required considerably more computational power and time compared to simulations without it, as the HBAR required accurate 3-dimensional simulations of the field modes – compared to the qubit, where most of the complexity of the field modes (and thus, the areas that require fine meshing and higher computational load) is close to the surface.

As a result, it proved more effective to iterate through designs in the absence of the HBAR, accounting roughly for its effects on the system parameters and compensating for these effects. These effects are illustrated in Figures 3.7, 3.12 and 3.13. The effect of the HBAR on the E-field within the cavity can also be seen in Figure 3.14.

In particular, the effects of the HBAR can be summarised as:

- The HBAR provides an additional capacitive coupling between the qubit pads, thus decreasing E_C and consequently the qubit frequency and anharmonicity. We see a decrease in ω_q of roughly 1–1.5 GHz, and a decrease in α of about 80 MHz.

- Similarly, the capacitive coupling of the HBAR also decreases the resonator frequency. This effect can be mitigated by minimising the overlap of the HBAR and the resonator – which is the exact purpose of the long straight section between the qubit and the rest of the meander resonator. For our design, we see a decrease in ω_r of roughly 0.3 GHz.

- The effect of the HBAR on the qubit-CPW coupling is more subtle. In the absence of the HBAR, we observe the relationships $l_{res} \propto 1/g$ and $l_{con} \propto g$, allowing us to reliably fix our coupling by fixing the ratio of these lengths. The HBAR contribution, however, adds a higher-order term to this calculation, which has not yet been empirically obtained.

3.4 Current Design

After iterating through designs and tuning qubit and resonator parameters until they were in accordance with the design specifications (Table 3.1), we finalised the geometry of our qubit design.

3.4.1 Tuning Workflow

We first provide the 'tuning workflow' – the order in which we changed variables to obtain desired parameters – in order to facilitate future work in this project. We note that this workflow was informed by the strictness (or lack thereof) of our design specifications.

1. We tune the anharmonicity of the qubit, using the pad dimensions. This is easily done without the HBAR using Qiskit Metal and its Ansys renderer; we perform checks after every few iterations to confirm that the actual anharmonicity, as well as g_{an}, are within specifications.

2. We confirm the qubit frequency. For developing our current geometry, we worked with a fixed Josephson inductance $L_{\text{J}} = 10\text{nH}$ – however, subsequently, we varied L_{J} in order to calibrate our junction fabrication process. L_{J} influences the qubit frequency, which informs our choice of resonator geometry, and the resulting Δ and χ.

3. We tune the resonator length, based on the desired detuning Δ.

4. We tune the connector length based on the desired dispersive shift χ. Depending on our purposes, it can be simpler to tune g, obtaining it from χ through EPR analysis. It is also possible to fix a desired range of values for g – which can be done to first order by fixing the ratio $l_{\text{con}}/l_{\text{res}}$ – and tune both Δ and χ simultaneously, which is faster but less precise.

3.4.2 The Standard Pocket Transmon

The standard transmon design is illustrated in Figures 3.1 and 3.6. The finalised geometry is given here in Table 3.2.

Design Variables	Values
Pad width	300 um
Pad height	180 um
Pad gap	100 um
Antenna length	500 um
Antenna radius	35 um
Resonator length	8.2 mm
Connector length	146 um
TL coupling length	250 um

Table 3.2: A possible set of design parameters. We note that the resonator and connector lengths are chosen to fit the case of a qubit with a bonded HBAR, and with a junction inductance of 9.7 nH. The TL coupling length is obtained from experiments.

The qubit dimensions are kept constant for every further iteration of the design (that is, for changing L_J). The resonator, following the methodology of Section 3.4.1, is tuned separately once the qubit frequency is known – and whether the qubit is intended to be measured with or without an HBAR present. We note that the intention was to tune the connector length along with the resonator; however, because of a fabrication error, we used a constant connector length of 180 um for all devices.

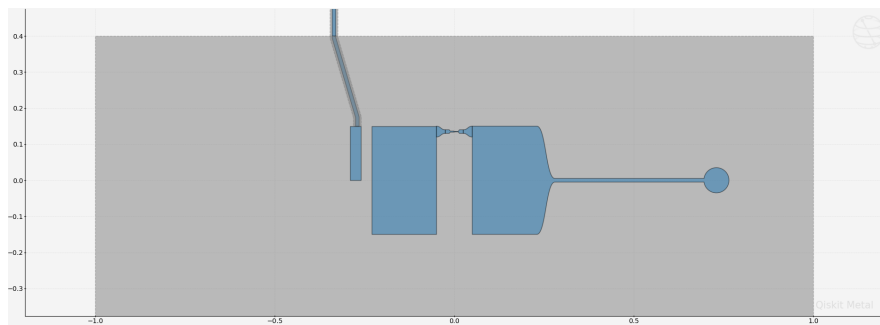### 3.4.3 The Shifted-Junction Transmon

Figure 3.15: An illustration of the shifted-junction transmon.

We also developed a second design to address a problem with the standard pocket transmon. While it suffices for most of our purposes, its geometry – with the junction right at the center of the design, between the two pads – makes it difficult to introduce elements that affect the junction, such as flux bias lines, without substantially changing qubit properties. We decided to make a simple modification to the transmon design: moving the junction close to one side of the gap. The resulting design is illustrated in Figure 3.15.

Design Properties	Standard	Shifted-Junction
Qubit frequency, f_q	4.76 GHz	4.86 GHz
Anharmonicity, α	193 MHz	200 MHz
Qubit-CPW coupling, g	150 MHz	151 MHz
Qubit-HBAR coupling, g_{an}	153 kHz	150 kHz

Table 3.3: Qubit properties for the standard transmon and shifted-junction transmon, for the parameters in Table 3.2.

The shifted junction transmon uses the same qubit parameters as the regular transmon, and has very similar properties, as we demonstrate in Table 3.3. As such, it offers no visible disadvantages, and we proceeded to fabrication with both designs.

Chapter 4

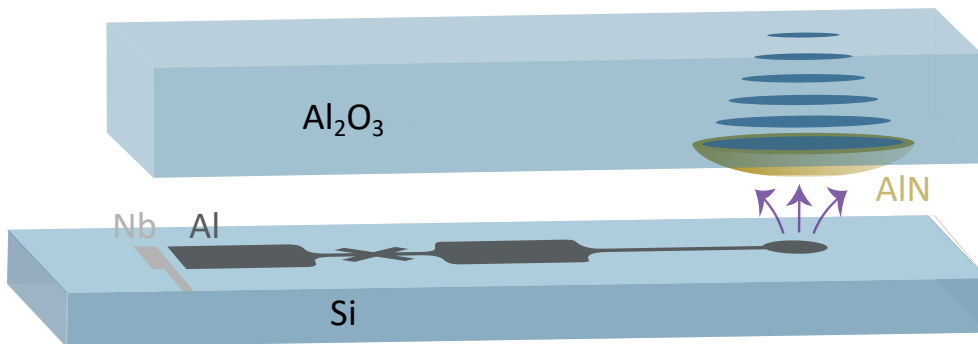# Fabrication & Measurement

4.1 Device Overview

Figure 4.1: Adapted from Banderier, Drimmer, Chu (2023) [1]. The setup described here is very similar to the setup in the cited paper, but uses silicon as the qubit chip substrate, aluminum for the qubit components, and niobium for the remaining (resonator and ground plane) conductors.

The devices produced as part of this project all use niobium films on silicon wafers for all circuit components (except qubits). This combination is a standard in the field of superconducting circuit fabrication, with quality factors of 5×10^6 having been achieved [19]. For our qubits, we use Al on silicon, as aluminum can be easily deposited through evaporation, and Al/AlOx/Al junctions can be created as part of this process. Making our qubits entirely of Al also means we do not have to perform an additional 'bandaging' step [20]. For our mechanical and piezoelectric components, we continue to use sapphire HBARs and AlN domes.

4.1.1 The Mix-Chip Design

As we have two different qubit designs to test, and resonators to characterise, we work with a mix-chip design. This design consists of:

- a reference resonator,

- a resonator coupled to the standard transmon design,

- a resonator coupled to the shifted-junction transmon design,

- a resonator coupled to a 'basic' design that resembles the standard transmon, but has no antenna.

The two qubits with antennas are designed to be used with an HBAR, while the 'basic' qubit is designed to used and measured in the absence of an HBAR. The GDS file of a single chip design is pictured in Figure 4.2.
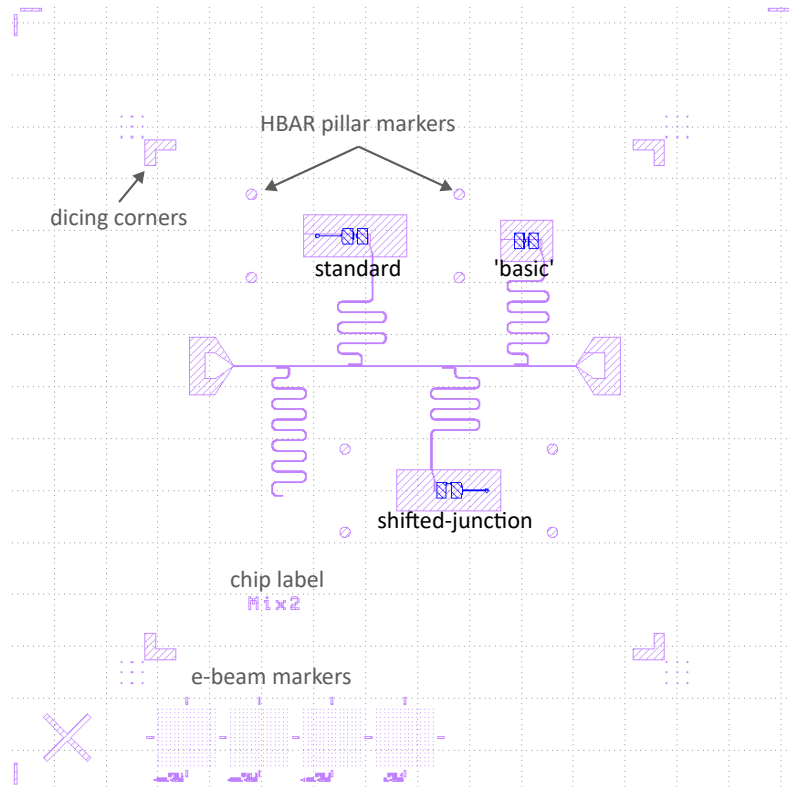
Figure 4.2: GDS file of a single mix-chip design. The three qubits and pockets are marked, as are the dicing corners, and the spaces left for flip-chip bonding of HBARs around the standard and shifted-junction transmons. All other features (including the markers at the edge of the design and outside the dicing corners) are for E-beam alignment.

We produced 8 of these chips, with different qubit frequencies given by different junction inductances. The qubit geometries are constant across all

chips, and the same parameters are used for the 'basic' qubit as the other qubits – with the exception of the *fingerwidth*, which influences the junction inductance, and is explored in more detail in Section 4.2.3.

4.2 Fabrication Methods

We provide a brief overview of the techniques used to create a device based on the designs developed during this project. We were primarily involved in the resonator fabrication steps; thin film deposition was performed by the Quantum Device Lab, and qubit fabrication was performed by other members of the Hybrid Quantum Systems group. The steps involved are summarised in Figure 4.3.
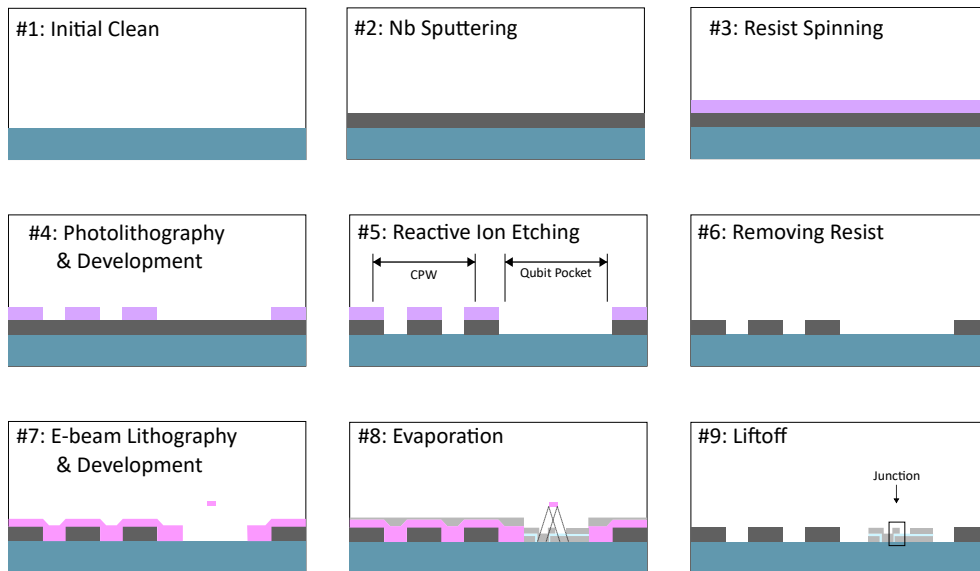

Figure 4.3: A summary of the fabrication process for our devices. We mark the locations of the CPW and the qubit for clarity. No components in this picture are to scale.

4.2.1 Resonator Fabrication

We first fabricate the resonator components, along with markers required for subsequent stages, out of niobium. We begin with single-side polished silicon wafers; following a cleaning step with hot NMP, we deposit a niobium film using magnetron sputtering (panel 2 of Figure 4.3). We work with film thicknesses of approx. 150 nm on wafer thickness of 535 um. This work was performed for us by Bahrami Panah Mohsen, Alexander Flasby, and the Quantum Device Lab.

Once having obtained our Nb-deposited wafers, we pattern the resonator and qubit pocket using direct-write laser lithography. The direct-write method,

performed using the Heidelberg DWL66+, allows us to operate without a photomask – instead, we provide GDS files directly to the laser writer, which patterns them using a laser beam and acousto-optic modulators and deflectors [21]. However, this method came with a number of additional challenges:

- The DWL66+ is prone to creating 'steps' along straight resonator lines, due to the line-by-line operating mechanism of the laser writer.

- Our initial laser lithography recipe struggled to produce the fine features needed for our device pattern – and, especially, the e-beam lithography alignment markers pictured in Figure 4.2, which are necessary for the qubit fabrication step.

- Our initial recipe was also prone to underdeveloped segments connecting the resonator or transmission line to the ground plane.
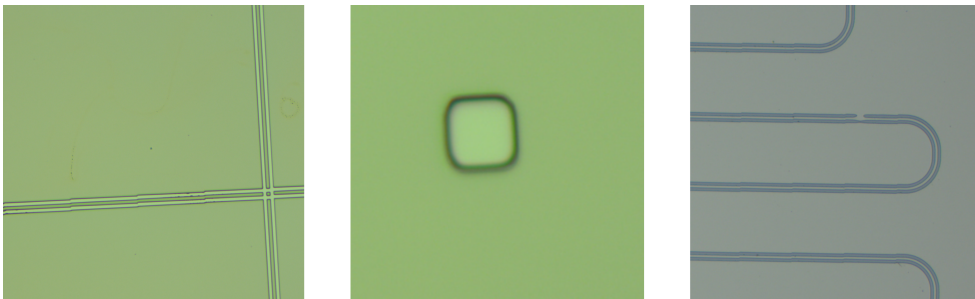
These issues are illustrated in Figure 4.4.

Figure 4.4: Defects encountered in initial fabrication attempts. *Left:* Steps visible in calibration pattern of two crossing transmission lines. *Center:* Rounded edges of (smallest) alignment marker. The marker needs to be a sharp square of dimensions 10 um by 10 um, but had rounded edges and dimensions of approximately 12 um by 12 um. *Right:* Incomplete development in one of the CPWs, leading to a short.

Correcting these defects required us to perform a calibration of the DWL66+, adjusting laser power and focus as well as the development time. In our final recipe, we reduce laser power (from 46 to 27 mW) and increase development time (from 4 mins 30 s to 5 mins), which resolved all of the aforementioned defects. We note that the DWL66+ also required regular calibration of the 'Expodie: AOD0' parameter, which controls vertical displacement of the laser writer between (vertical) stripes; miscalibration of this parameter is one of the factors that contributes to the steps in Figure 4.4.

After creating the pattern through laser lithography, we transfer the pattern onto the niobium substrate using reactive ion etching (plasma etching) [22]. Plasma etching characteristically has an anisotropic etching profile, allowing us to transfer patterns precisely and without undercutting. We work with

an SF_6-based recipe to exploit the volatile nature of niobium and silicon fluorides. To make sure that etching of all features is complete, we use endpoint detection (based on the reflectivity of niobium vs silicon), and perform an overetch of 20 seconds. Veering on the side of overetching ensures that all our features are properly formed, with no excess niobium present, at the cost of slightly modifying the capacitances (per unit length) of our various lines.

One of the defects visible in the final device was, unfortunately, introduced in this step, and is pictured in Figure 4.5. We believe these defects, which appear across the chip (and in some occasions, short out CPWs or transmission lines), arise because of dust on the wafer prior to plasma etching, and can be resolved by careful blowing prior to resist spinning and etching. We initially considered that they were flakes being transfered across the chip, but ruled out that possibility after reviewing darkfield images of these defects crossing resonators.
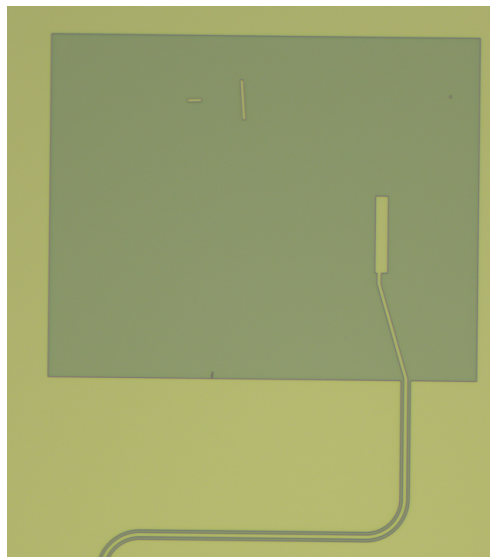
Figure 4.5: The qubit pocket after plasma etching, but before qubit fabrication. We can clearly see small segments of niobium in the pocket that were not present during photolithography.

4.2.2 Resonator Measurements

We also discuss measurements made at the start of the project to characterise niobium-on-silicon resonators, as these measurements inform us on certain design parameters. Firstly (as discussed in Section 3.3.2), we expect to be able to tune the resonator frequency by changing the resonator length. Secondly, we wish to understand what quality factors can be achieved with our current recipes, in order to estimate our Purcell losses (as discussed

in Section 2.3.4) and in order to ensure that we operate in the overcoupled regime (as discussed in Section 2.2.3 – if we operate in the undercoupled regime, it will become more difficult to detect our resonators).

When characterising superconducting circuit resonators, we must account for the interaction between measurement power and resonator properties. Recalling Equation 2.16 and 2.17, we note that the frequency is a function of circuit inductance; in the case of a superconductor, this inductance L_l is given as a combination of the geometric inductance L_l^m (mediated by magnetic fields) and the kinetic inductance L_l^k [10]. While the former is temperature independent, and is defined by the geometry of the system, the latter is temperature-dependent [23] – in particular, we have

$$L_l^k = \frac{\hbar}{\sigma_n \pi \Delta_{sc} \tanh\left(\Delta_{sc}/2k_B T\right)} \frac{l}{A},$$

for a superconductor with length l, cross-section A, normal state conductivity σ_n, and superconducting gap Δ_{sc}. This relationship suggests that our resonator frequencies would decrease with increasing measurement power. However, with niobium and our film thicknesses, we maintain a low ratio of L_l^k/L_l^m, minimising the impact of changing kinetic inductance; as a result, our frequencies do not change considerably with power, as seen in Figure 4.6.
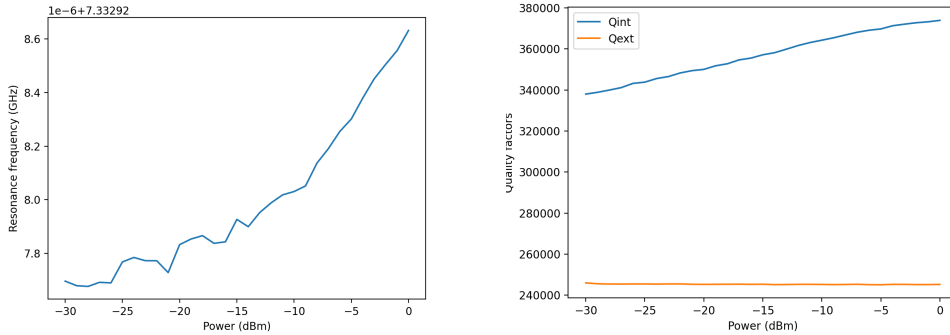

Figure 4.6: An example of resonator characterisation, illustrating power dependencies. *Left:* Measurements of frequency for varying measurement power. We note the y-axis scaling; the relative uncertainty here is 1.5×10^{-7}. *Right:* Measurements of internal and external quality factor, obtained by circle fitting [11]. We see that Q_{ext} is constant, while Q_{int} increases.

The intrinsic losses of the resonator show a much larger power dependence. A superconducting circuit system possesses a number of loss mechanisms, but we consider two-level systems (TLS) losses in particular [24, 25]. The TLS model was initially developed to explain the low-temperature behaviour of amorphous solids [26], but can also be applied to regions on a super-conducting device with amorphous solids, such as oxide films. This model proposes that, in an amorphous solid, there exist atoms that sit in one of

two energetically-asymmetric minima separated by a potential barrier. When the resonator electric field couples to these TLS, they become additional relaxation channels for the resonator mode. The main characteristic of this loss mechanism is that, unlike other dielectric loss models, TLS losses *decrease* with increasing measurement power, as these systems become saturated; this results in increasing Q_{int} for increasing power, which is exactly the trend we see in Figure 4.6.

As our dispersive shift scheme operates with the assumption that the cavity is in the ground state, we characterise our resonators at low input power. Two chips were fabricated, each with 4 resonators side-coupled to a central transmission line. The results are given in Figures 4.7 and 4.8. From the fits, we conclude that both resonator frequency and external quality factor can be reliably tuned using their respective design parameters; furthermore, we converge on a desired coupling to the transmission line, setting $Q_{\text{ext}} \approx 6 \times 10^5$ such that our resonators are always overcoupled.
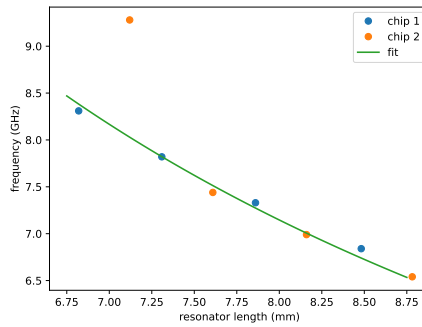

Figure 4.7: Frequencies against resonator length. The fit uses a basic reciprocal function $y = A/x$ (based on the relation in Equation 2.16), and excludes the outlier at 9.28 GHz. These frequencies are measured with an input power of -30 dBm (decibel-milliwatts) for chip 1, and -50 dBm for chip 2, as there were issues with the measurement setup for the first chip.
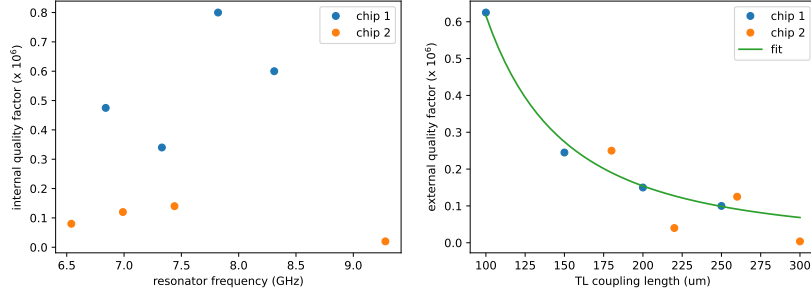
Figure 4.8: Plotting internal and external quality factors. These quality factors are obtained at -30 dBm. *Left:* Internal quality factors against frequency. We note, again, the outlier at 9.28 GHz. *Right:* External quality factor against TL coupling length. The fit uses a reciprocal function $y = A/x^2$ (based on the relation in Equation 2.21).

4.2.3 Qubit Fabrication

We briefly describe the qubit fabrication process for completeness. The qubit patterns are created using E-beam lithography, and aligned using the markers created during resonator fabrication (visible in Figure 4.2). We perform argon ion milling to remove oxide layers and excess niobium/resist from the chip, and then use shadow evaporation to form our qubit structures and junction. All of this work was done with the help of Marius Bild and Andraz Omahen, and with the assistance of the Binnig and Rohrer Nanotechnology Center (BRNC) cleanroom staff.

We note that the Plassys evaporator used for qubit fabrication had issues before and during our chip fabrication, notably with maintaining internal pressures and with withdrawing the wafer (which was partially damaged during this stage). There were also other issues before dicing (the wafer was quite fragile, and broke while spinning dicing resist). While this fracture did not visibly damage any of the devices on the wafer (which includes the fingerwidth test discussed in Section 4.2.3 and the final device in Section 4.4), it is possible that they affected the properties of the fingerwidth test chip and the final device chip.

Junction Design

We recall that one of the qubit design parameters discussed in Section 3.3 is the *junction inductance L_J*. In a physical device, this junction inductance is controlled by the dimensions of the junction; in our devices, we tune this by changing the overlap between the two fingers of the qubit pads (referred to as the *fingerwidth*), as illustrated in Figure 4.11.
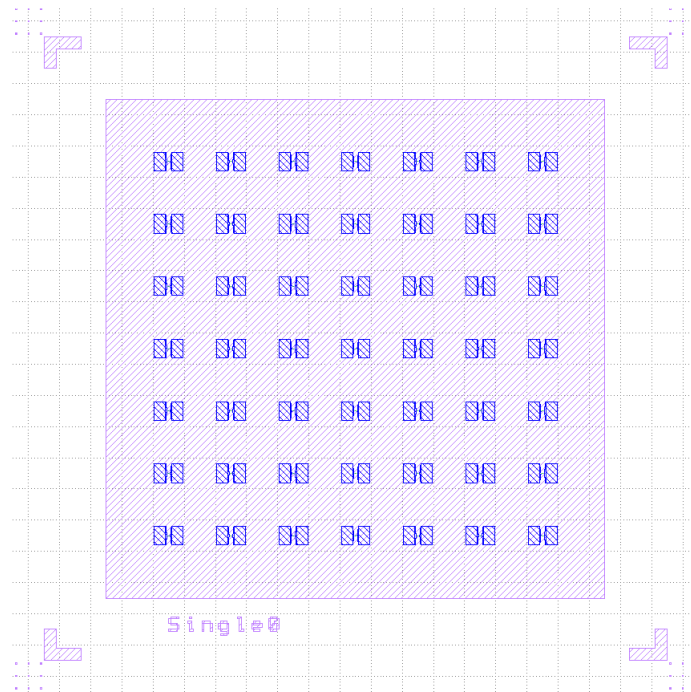
Figure 4.9: The fingerwidth test chip design, with 49 junctions and fingerwidths ranging from 100 to 210 nm.
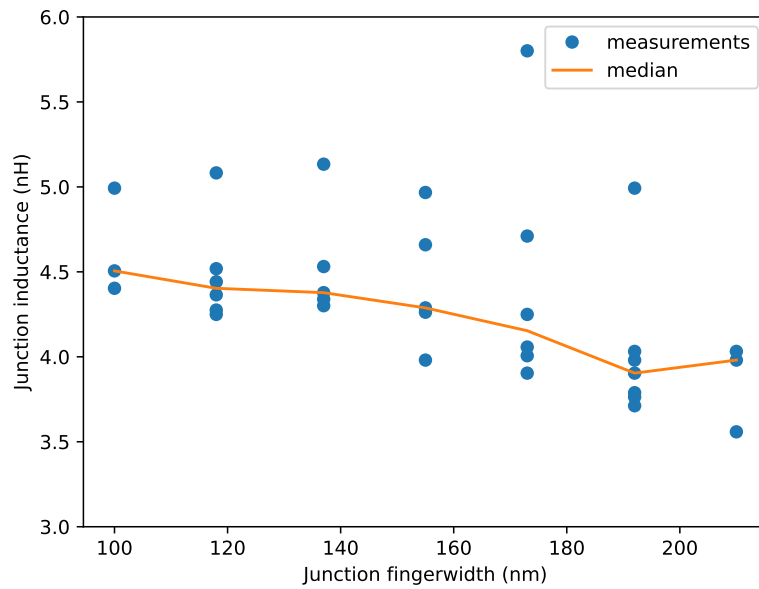

Figure 4.10: Measurements of junction inductance against fingerwidth. We see a weak trend in junction inductances, with several outliers. 10 of the junctions measured were also either open (no connection) or shorted.
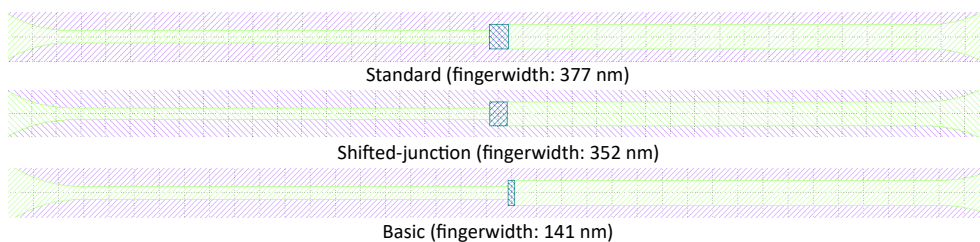
Figure 4.11: Fingerwidths of the three qubits in Figure 4.2. The fingerlength remains constant for all qubits, and is set at 480 nm.

The relationship between junction dimensions and junction inductance has been documented for other materials in the Hybrid Quantum Systems group, but not yet for the combination of aluminum and silicon. We study this relationship by sweeping a range of fingerwidths (in both mix-chip designs and in separate test chips, one of which is pictured in Figure 4.9). We produce these test chips as part of the same wafer as the mix-chips because of time constraints, so we pick our junction dimensions for the qubits based on data for aluminum-on-sapphire qubits.

For each fabricated junction, we use a DC probe to measure the *normal state resistance* [27]. The normal state resistance can be related to the critical current by the following equation,

$$R_{\mathrm{n}} = \frac{\pi \Delta_{\mathrm{sc}}}{2 e I_{\mathrm{c}}},$$ (4.1)

where Δ_{sc} is the superconducting gap of aluminum at 0 K. This can be related back to the junction inductance through Equation 2.9. Considering the relationship between the junction dimensions and the critical current, we expect that an increase in fingerwidth will lead to a decrease in junction inductance. Unfortunately, our measurements do not strongly support this hypothesis – as illustrated in Figure 4.10, we only see a weak trend in junction inductances.

4.3 Final Device

Eight mix-chip devices were designed, with a range of expected junction inductances, qubit frequencies, and resonator frequencies. Two of these chips were successfully fabricated, and one of them – referred to in notes as chip Mix2 of wafer WCPW05 – is currently being measured. Unfortunately, due to delays with the evaporator, these measurements could not be completed in time for the thesis deadline. However, in the hopes of validating (or otherwise) our designs, we present the expected properties of Mix2, and some preliminary results obtained through DC probing of the qubit junctions.

Design Properties	Standard	Shifted-Junction	Basic
Junction inductance (nH)	6	6.43	12
Qubit frequency (GHz)	7.59 (bare) 6.07 (bonded)	7.49 (bare) 5.97 (bonded)	5.82 (bare) -
Anharmonicity (MHz)	- 182 (bonded)	- 187 (bonded)	256 (bare) -
CPW frequency (GHz)	8.61 (bare) 8.32 (bonded)	8.37 (bare) 8.07 (bonded)	7.67 (bare) -
Qubit-CPW coupling (MHz)	- 249 (bonded)	- 239 (bonded)	196 (bare) -
Dispersive shift (MHz)	- 4.11 (bonded)	- 4.44 (bonded)	5.03 (bare) -
Qubit-HBAR coupling (kHz)	209	206	-

Table 4.1: Expected properties of the device. We calculate properties in the cases of a bare (with no HBAR) and bonded (with an HBAR bonded) chip. In some cases – notably, the dispersive shift of the standard and shifted-junction transmons – we do not provide values, as the EPR analysis does not converge well for these values of junction inductance and detuning.

At the end of the fabrication process, Mix2 and one other (Mix6) had all three qubits seemingly functional. We checked this by DC-probing the individual qubits, and measuring the resistance – which, as discussed in Section 4.2.3, gives us the junction properties. If the junction was not formed correctly, we measure 0 resistance (shorted) or infinite resistance (open). We considered both chips for measurement, but selected Mix2 based on the normal state resistances obtained.

As we can see from Table 4.2, the junction inductance of the standard transmon in Mix2 is significantly higher than expected, but the other junctions inductances do not deviate too strongly from their expected values. Additionally, we note that the shifts in qubit frequencies for the standard and shifted-junction transmon will only improve their properties in the bare measurement case, while the basic transmon will suffer increased (but still acceptable) Purcell losses. However, we also observe that this data disagrees with the data from the fingerwidth sweeps in Figure 4.10, so it is unclear whether these measurements can be used as a basis for junction design.

Mix2 also has a defect in the reference resonator, but as the mix-chip design has three other resonators we can characterise, we proceeded to mount and

Chip Properties	Standard	Shifted-Junction	Basic
Fingerwidth (nm)	377	352	141
Expected junction inductance (nH)	6	6.43	12
Measured junction inductance (nH)	10.40	6.46	10.28
Corrected qubit frequency (GHz)	5.81	7.40	6.28

Table 4.2: Corrected junction and qubit properties after DC probing. We obtain qubit frequencies using the simulated charging energy E_C, which is itself obtained through the approximation $\alpha \approx E_C$.

cool down this device. We also provide some pictures of the qubits on Mix2 (Figures 4.12 through 4.14), as well as the shorted resonator (Figure 4.15).

chip2-qubitB | FIRST-Wetchem | 10x   100µm
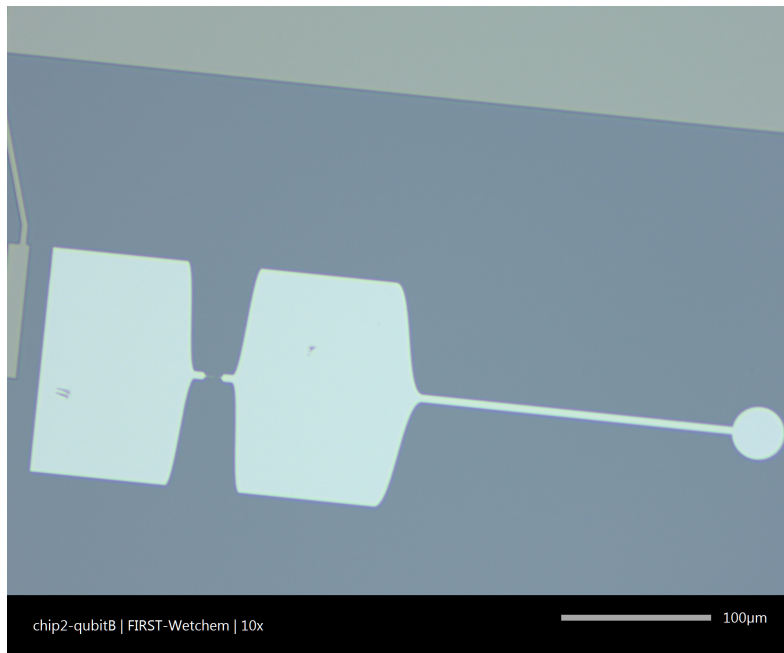
Figure 4.12: The standard transmon on Mix2.

chip2-qubitA | FIRST-Wetchem | 5x   200µm
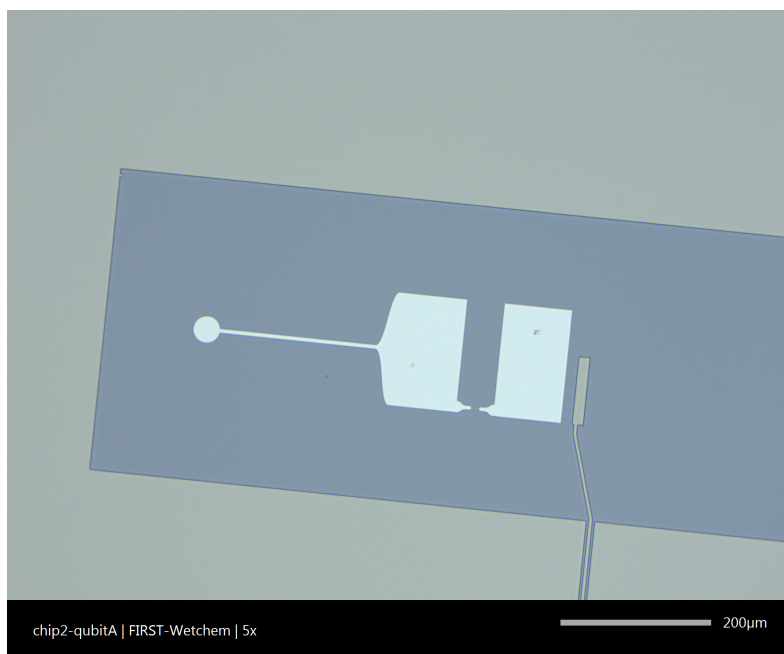
Figure 4.13: The shifted-junction transmon on Mix2.

49

chip2-qubitC | FIRST-Wetchem | 10x   100µm
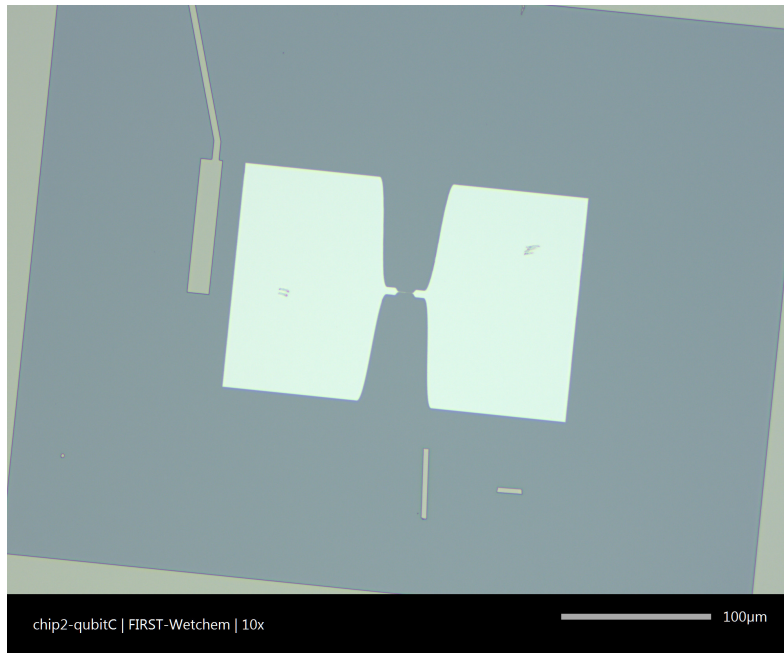
Figure 4.14: The 'basic' transmon on Mix2. This is the same chip section pictured in Figure 4.5, and has the same defects.

chip2-res | FIRST-Wetchem | 10x   100µm
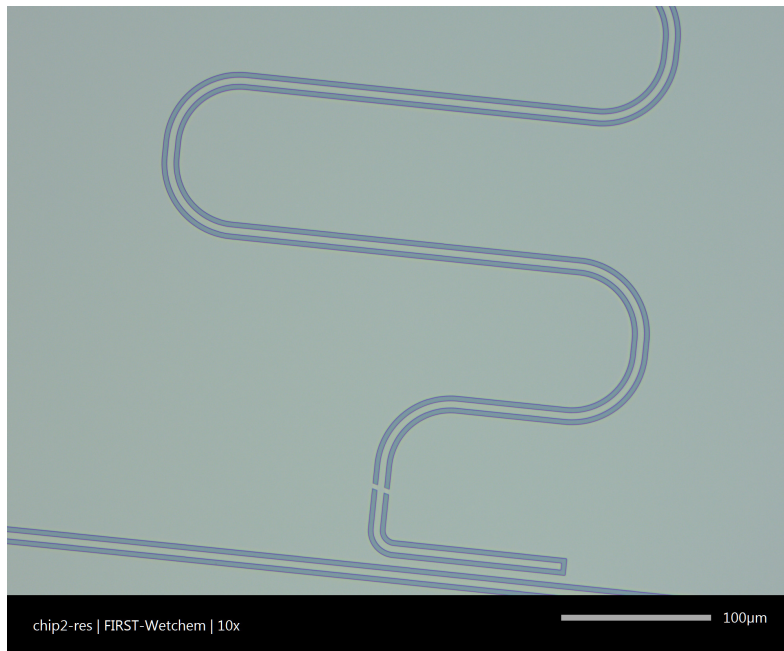
Figure 4.15: A portion of the reference resonator on Mix2, showing the defect connecting the central conductor to ground. We believe this is the same sort of defect described in Section 4.2.1 – that is, unetched niobium from dust on the wafer during etching.

4.4 Device Measurements

Following the completion of this project, we were able to finish measurements on the device, and characterise the qubits and resonators. The results are presented in Table 4.3.

Chip Properties	System 1	System 2	System 3
CPW frequency (GHz)	7.25	7.55	7.79
Qubit frequency (GHz)	6.57	6.61	6.16
Qubit T1 (us)	0.938	0.829	1.03
Qubit T2 (us)	0.667	0.398	0.678

**Table 4.3:** Resonator frequency and qubit properties. It was initially unclear which qubits gives rise to which modes, so we refer to them in order of increasing frequency.

Comparing the results of Table 4.3 to Tables 4.1 and 4.2, we note that both the qubit and resonator frequencies are different from expected. This prompted us to revisit the simulations of all eight mix-chip devices we started with. In particular, we considered that there had been a mixup between devices during the dicing process, so we reviewed the frequencies of the readout resonators on all chips, the results of which are presented in Figure 4.16.

Figure 4.16 reinforces the idea that the device being measured is not Mix2 at all, but Mix4, a device with somewhat different properties. It is likely that this mixup happened between dicing and mounting, as the chip labels were removed during the dicing process. This conclusion, however, would be best verified by checking the resonator lengths of the device using optical microscopy, once it can be removed from the fridge. We also provide the simulated properties of Mix4 in Table 4.4, considering only the bare (no HBAR bonded) case.

Design Properties	Standard	Shifted-Junction	Basic
Junction inductance (nH)	9	7.86	10
Qubit frequency (GHz)	6.25	6.76	6.36
Anharmonicity (MHz)	278	319	305
CPW frequency (GHz)	7.13	7.66	8.29
Qubit-CPW coupling (MHz)	200	221	204
Dispersive shift (MHz)	21.8	28.5	5.89

Table 4.4: Expected properties of Mix4, comparable to the properties of Mix2 in Table 4.1. We only provide the properties in the absence of a bonded HBAR for compactness.

Additionally, Figure 4.16 gives us the mean absolute error in frequency, 247 MHz ($\sim$ 4% error) across both resonators and qubits. The error in
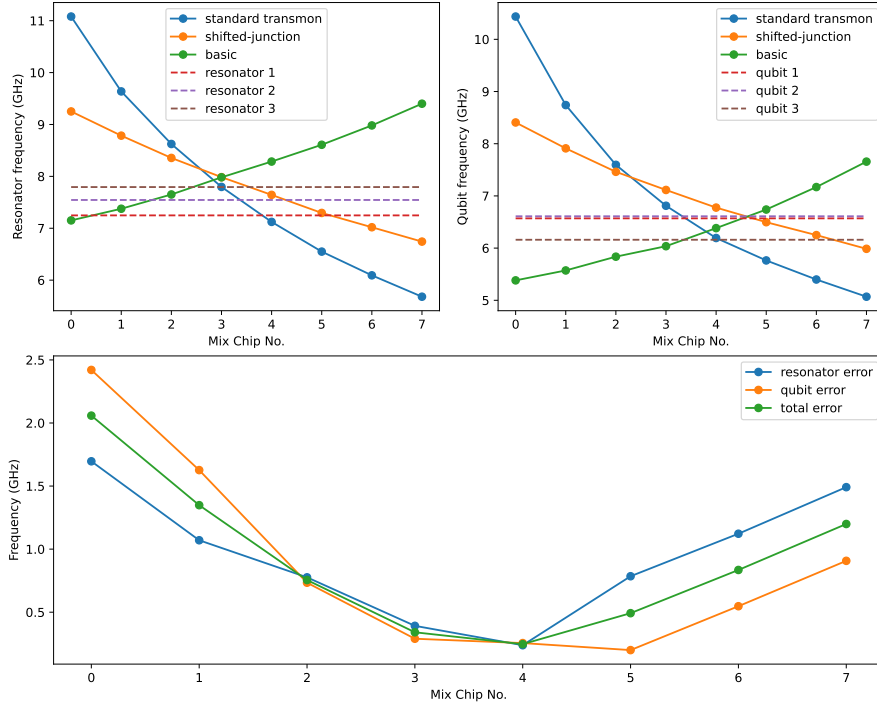
51

Figure 4.16: Simulated resonator and qubit frequencies for all eight devices vs. observed frequencies on the final device. *Left:* Simulated frequencies for resonators, labelled by the qubit they are coupled to. The dashed lines mark the observed frequencies. *Right:* Simulated frequencies for qubits, labelled by design. The dashed lines mark the observed frequencies. *Bottom:* Mean absolute deviation of each device's predicted frequencies from the observed frequencies, separated into deviation in resonator, qubit and all frequencies. This assumes that Systems 1, 2, and 3 are chosen (as being the standard, shifted-junction or basic transmon) to minimise the total error.

resonator frequencies is considerably larger than the deviations observed in the resonator-only chips discussed in Section 4.2.2; the cause of this remains to be explained. Finally, in looking for the minimum deviation, we also obtain probable guesses at which designs correspond to which qubit and resonator modes: we can identify System 3 ($f_r = 7.79$ GHz, $f_q = 6.16$ GHz) as the basic transmon, and we identify Systems 1 and 2 as the standard and shifted-junction transmons respectively.

Additionally, T_1 and T_2 times [8] were measured for all three qubits. As illustrated in Table 4.3, they are all very low, lower than the 10 us threshold we had hoped to achieve in this project. These low coherence times can be partially explained through the strong Purcell decay effect in the standard and shifted-junction transmon designs. They were designed to operate with a bonded HBAR, and compensate for its effects (as discussed in Section 3.3.3); in its absence, we have very low detunings, and thus a high Purcell decay. However, this does not explain the short lifetime of the basic transmon, which was designed to have a Purcell decay rate according to design specifications.

Finally, the device appeared to be poorly thermalised: measurements of the resonator state population (given in Figure 4.17) concluded that the resonator was at 320 mK – much higher than the desired temperature of $\sim$ 20 mK. This likely had a additional effect on qubit lifetimes.
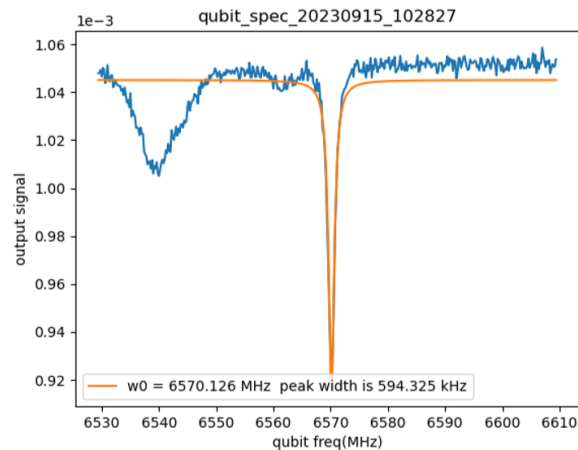
Figure 4.17: Measuring the resonator Fock state populations using the qubit dispersive shift. The fitted peak corresponds to the resonator ground state, and the peak to the right the resonator Fock state $|1\rangle$. The ratio between the depths allows us to extract the temperature of the resonator thermal state.

Figure 4.18: Rabi oscillations measured on the qubit mode at 6.57 GHz.

Additionally, we measured clear Rabi oscillations on the standard transmon, confirming its properties as a qubit and our ability to perform coherent control on the device. These measurements are also limited by the very short lifetimes, but fit well to theoretical behaviours for short pulse times.

Chapter 5

Outlook

The objective of this project was to help establish a 2D circuit platform for the cQAD experiments performed by the Hybrid Quantum Systems group. Across the course of this project, we have explored tools f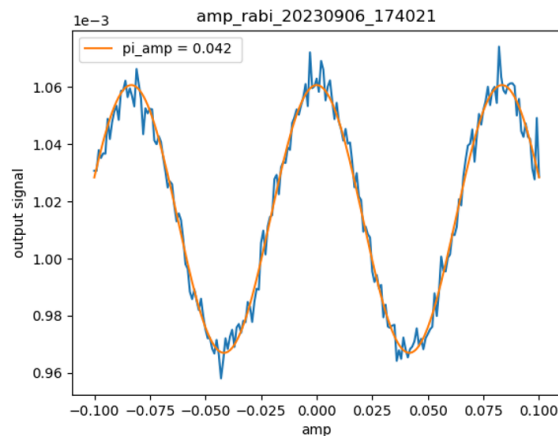or superconducting circuit design and simulation, and established a design process for developing new devices. We have fabricated new devices using an industry standard combination of materials, and in doing so we have embarked on a 'proof of concept' project to demonstrate the viability of these platforms. We argue that the measurements of our first device do support the feasibility of this platform, but show that there is much improvement to be gained by further optimisation of the design and fabrication process.

As with all proofs of concept, there are many aspects of this project that future research can build upon. From the fabrication side, we note that the properties of aluminum-on-silicon junctions, and the loss rates of niobium-on-silicon resonators, remain to be fully studied. Additionally, there have been many advances in the field of microfabrication that would improve our process – for example, etching to remove oxide layers [19], using niobium to construct a larger portion of the qubit (and bandaging with Al/AlOx/Al junctions) [20], and exploring tantalum-on-sapphire devices [28], could all improve our coherence times.

From the design side, a 2D circuit platform creates many new opportunities. We were constrained by the Purcell decay mechanism in this project, but it would be a natural next step to add Purcell filters to our circuits. Our mix-chips also open the door to qubit multiplexing, and illustrate the challenges of circuit design in the presence of an HBAR. During the course of this project, we also noted that it was possible to achieve higher qubit-HBAR coupling factors (up to 1 MHz) using *grounded qubits* (qubits where the junction connects one charge island and the ground plane, rather than two charge islands); while HBAR-mediated decoherence mechanisms remain poorly understood, this remains a potential avenue to explore.

Bibliography

1. Banderier, H., Drimmer, M. & Chu, Y.
   Unified simulation methods for quantum acoustic devices. 2023.
   arXiv: 2301.05172 [quant-ph].

2. Krass, M.-D. *et al.* Force-Detected Magnetic Resonance Imaging of
   Influenza Viruses in the Overcoupled Sensor Regime.
   Phys. Rev. Appl. **18,** 034052. doi:10.1103/PhysRevApplied.18.034052.
   https://link.aps.org/doi/10.1103/PhysRevApplied.18.034052
   (3 Sept. 2022).

3. Mahboob, I. & Yamaguchi, H.
   Bit storage and bit flip operations in an electromechanical oscillator. en.
   Nat Nanotechnol **3,** 275–279 (Apr. 2008).

4. Chu, Y. *et al.* Creation and control of multi-phonon Fock states in a bulk
   acoustic-wave resonator. *Nature* **563,** 666–670. ISSN: 1476-4687.
   doi:10.1038/s41586-018-0717-7.
   https://doi.org/10.1038/s41586-018-0717-7 (Nov. 2018).

5. Von Lüpke, U. *et al.* Parity measurement in the strong dispersive regime
   of circuit quantum acoustodynamics. *Nature Physics* **18,** 794–799.
   doi:10.1038/s41567-022-01591-2.
   https://doi.org/10.1038%2Fs41567-022-01591-2 (May 2022).

6. Bild, M. *et al.*
   Schrödinger cat states of a 16-microgram mechanical oscillator.
   Science **380,** 274–278. doi:10.1126/science.adf7553. eprint:
   https://www.science.org/doi/pdf/10.1126/science.adf7553.
   https://www.science.org/doi/abs/10.1126/science.adf7553
   (2023).

7. Blais, A., Grimsmo, A. L., Girvin, S. & Wallraff, A.
   Circuit quantum electrodynamics. *Reviews of Modern Physics* **93.**

doi:`10.1103/revmodphys.93.025005`.
`https://doi.org/10.1103%2Frevmodphys.93.025005` (May 2021).

8. Krantz, P. *et al.* A quantum engineer's guide to superconducting qubits.
Applied Physics Reviews **6,** 021318. doi:`10.1063/1.5089550`.
`https://doi.org/10.1063%5C%2F1.5089550` (June 2019).

9. Roth, T. E., Ma, R. & Chew, W. C.
An Introduction to the Transmon Qubit for Electromagnetic Engineers.
2021. arXiv: `2106.11352 [quant-ph]`.

10. Göppl, M. *et al.*
Coplanar waveguide resonators for circuit quantum electrodynamics.
Journal of Applied Physics **104.** doi:`10.1063/1.3010859`.
`https://doi.org/10.1063%2F1.3010859` (Dec. 2008).

11. Rodrigues, I. C., Bothner, D. & Steele, G. A. Coupling microwave
photons to a mechanical resonator using quantum interference.
Nature Communications **10,** 5359. issn: 2041-1723.
doi:`10.1038/s41467-019-12964-2`.
`https://doi.org/10.1038/s41467-019-12964-2` (Nov. 2019).

12. Jaynes, E. & Cummings, F. Comparison of Quantum and Semiclassical
Radiation Theories with Application to the Beam Maser.
Proceedings of the IEEE **51,** 89–109. doi:`10.1109/PROC.1963.1664`
(Feb. 1963).

13. Boissonneault, M., Gambetta, J. M. & Blais, A. Dispersive regime of
circuit QED: Photon-dependent qubit dephasing and relaxation rates.
Phys. Rev. A **79,** 013819. doi:`10.1103/PhysRevA.79.013819`.
`https://link.aps.org/doi/10.1103/PhysRevA.79.013819`
(1 Jan. 2009).

14. Qiskit contributors.
Qiskit: An Open-source Framework for Quantum Computing. 2023.
doi:`10.5281/zenodo.2573505`.

15. Ansys Inc.
An Introduction to HFSS: Fundamental Principles, Concepts, and Use.
https://www.ansys.com/products/electronics/ansys-hfss. 2023. (2023).

16. Minev, Z. K. *et al.*
Energy-participation quantization of Josephson circuits.
npj Quantum Information **7,** 131. issn: 2056-6387.
doi:`10.1038/s41534-021-00461-8`.
`https://doi.org/10.1038/s41534-021-00461-8` (Aug. 2021).

17. Yuan, B., Wang, W., Liu, F., He, H. & Shan, Z. Comparison of Lumped Oscillator Model and Energy Participation Ratio Methods in Designing Two-Dimensional Superconducting Quantum Chips. *Entropy* **24.** ISSN: 1099-4300. doi:10.3390/e24060792. https://www.mdpi.com/1099-4300/24/6/792 (2022).

18. Knoll, J. Design and simulation of a superconducting qubit coupled to a bulk acoustic wave resonator. semester project report (D-PHYS, ETH Zurich, 2022). https://ethz.ch/content/dam/ethz/special-interest/phys/solid-state-physics/hyqu-dam/documents/semester-report-Jonathan-Knoll.pdf (2023).

19. Altoé, M. V. P. *et al.* Localization and Mitigation of Loss in Niobium Superconducting Circuits. *PRX Quantum* **3,** 020312. doi:10.1103/PRXQuantum.3.020312. https://link.aps.org/doi/10.1103/PRXQuantum.3.020312 (2 Apr. 2022).

20. Nersisyan, A. *et al.* Manufacturing low dissipation superconducting quantum processors. 2019. arXiv: 1901.08042 [quant-ph].

21. Heidelberg Instruments. DWL 66+ Fact Sheet. https://heidelberg-instruments.com/product/dwl-66-laser-lithography-system/. 2023. (2023).

22. Franssila, S. in *Introduction to Microfabrication* 127–141 (John Wiley & Sons, Ltd, 2010). ISBN: 9781119990413. doi:https://doi.org/10.1002/9781119990413.ch11. eprint: https://onlinelibrary.wiley.com/doi/pdf/10.1002/9781119990413.ch11. https://onlinelibrary.wiley.com/doi/abs/10.1002/9781119990413.ch11.

23. Schneider, C. M. F. Magnetic Coupling between Superconducting Circuits and a Cantilever. PhD thesis (University of Innsbruck, May 2021). https://iqoqi.at/_groups/images/group/gk/phd_theses/phd_schneider.pdf.

24. De Leon, N. P. *et al.* Materials challenges and opportunities for quantum computing hardware. *Science* **372,** eabb2823. doi:10.1126/science.abb2823. eprint: https://www.science.org/doi/pdf/10.1126/science.abb2823. https://www.science.org/doi/abs/10.1126/science.abb2823 (2021).

25. Martinis, J. M. *et al.*
    Decoherence in Josephson Qubits from Dielectric Loss.
    Phys. Rev. Lett. **95,** 210503. doi:10.1103/PhysRevLett.95.210503.
    https://link.aps.org/doi/10.1103/PhysRevLett.95.210503
    (21 Nov. 2005).

26. Phillips, W. A. Two-level states in glasses.
    Reports on Progress in Physics **50,** 1657.
    doi:10.1088/0034-4885/50/12/003.
    https://dx.doi.org/10.1088/0034-4885/50/12/003 (Dec. 1987).

27. I.C. Corveira Rodrigues. Coupling Harmonic Oscillators to
    Superconducting Quantum Interference Cavities.
    PhD thesis (Delft University of Technology, May 2021). https:
    //doi.org/10.4233/uuid:90c588b1-ebef-4ab8-b51f-b3221d8ad6cc.

28. Place, A. P. M. *et al.* New material platform for superconducting
    transmon qubits with coherence times exceeding 0.3 milliseconds.
    Nature Communications **12,** 1779. ISSN: 2041-1723.
    doi:10.1038/s41467-021-22030-5.
    https://doi.org/10.1038/s41467-021-22030-5 (Mar. 2021).

Declaration of originality

The signed declaration of originality is a component of every semester paper, Bachelor's thesis, Master's thesis and any other degree paper undertaken during the course of studies, including the respective electronic versions.

Lecturers may also require a declaration of originality for other written papers compiled for their courses.

_____

I hereby confirm that I am the sole author of the written work here enclosed and that I have compiled it in my own words. Parts excepted are corrections of form and content by the supervisor.

Title of work (in block letters):

Authored by (in block letters):
For papers written by groups the names of all authors are required.

Name(s):   **First name(s):**

....

....

....

....

With my signature I confirm that
− I have committed none of the forms of plagiarism described in the 'Citation etiquette' information sheet.
− I have documented all methods, data and processes truthfully.
− I have not manipulated any data.
− I have mentioned all persons who were significant facilitators of the work.

I am aware that the work may be screened electronically for plagiarism.

Place, date   **Signature(s)**

....

                                                ....

                                                ....

                                                ....

                                                ....

                                                For papers written by groups the names of all authors are required. Their signatures collectively guarantee the entire content of the written paper.